University of Glasgow
DEPARTMENT OF
AEROSPACE
ENGINEERING

EULER SIMULATIONS OF PITCHING DELTA WING AERODYNAMICS WITHIN WIND TUNNEL CONSTRAINTS

M. R. Allan

Dept. of Aerospace Engineering Technical Report 0114
November 2001

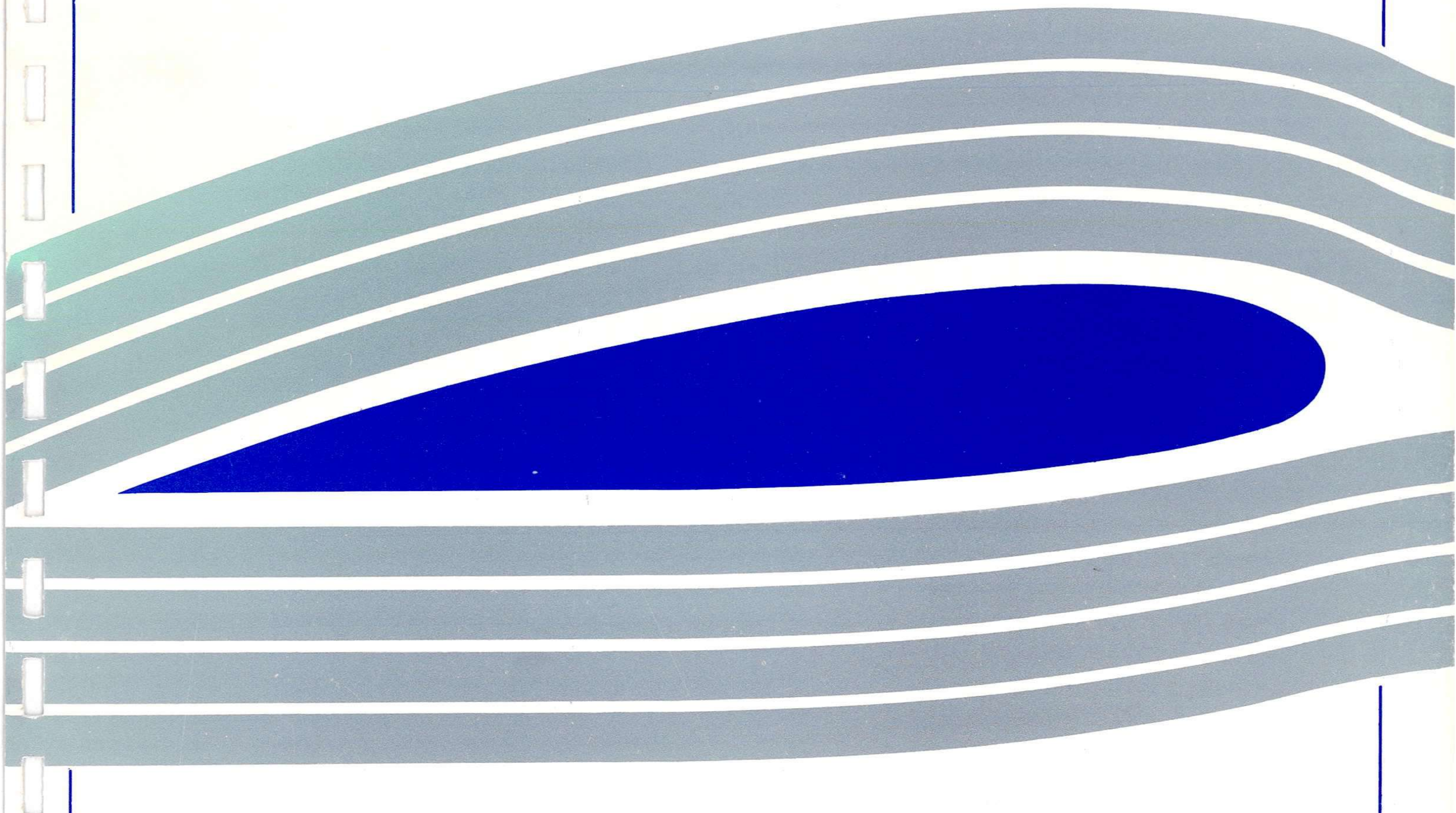

EULER SIMULATIONS OF PITCHING DELTA WING AERODYNAMICS WITHIN WIND TUNNEL CONSTRAINTS

M. R. Allan

Dept. of Aerospace Engineering Technical Report 0114
November 2001

EULER SIMULATIONS OF PITCHING DELTA WING AERODYNAMICS WITHIN WIND TUNNEL CONSTRAINTS

M. R. Allan

Department of Aerospace Engineering,

University of Glasgow,

Glasgow, G12 8QQ, U.K.

Department of Aerospace Engineering Technical Report 0114

November 16, 2001

Abstract

Euler simulations of a pitching delta wing within three wind tunnels (Square, 3x2, and 2x3 tunnels) have been performed. The solutions have been validated by comparing a farfield solution with experimental data. The steady solutions have shown that the presence of the wind tunnels promotes vortex breakdown, and that the side walls are the most influential. The presence of the side walls increases the suction on the surface of the wing, and shifts the vortex core inboards and upwards. The roof and floor have a lesser influence as was demonstrated by bringing the roof and floor closer to the wing surface (changing from the square tunnel to the 3x2 tunnel). It was concluded that the main effect causing the shift towards the apex of the breakdown location was an increase in the mean incidence of the wing.

As with the steady solutions, the unsteady solutions have shown that the 2x3 tunnel varies the breakdown locations the most, in comparison to those from the farfield solution. The greatest divergence of the breakdown locations from those of the farfield solution occurs on the downstroke of the motion. This is due to the fact that the wing leaves a state of high tunnel interference going to a state of lower interference.

Contents

List of Figures

Nomenclature

u	Velocity magnitude
S	Entropy
T	Temperature
h_o	Stagnation enthalpy
ω	Vorticity vector
$\mathbf{n}$	Direction normal to streamline
$\mathbf{N_s}$	Unit normal to surface
S/W	Wing span to tunnel width
S/H	Wing span to tunnel height
$\alpha(t)$	Instantaneous angle of attack
α_m	Mean angle of attack
α_0	Amplitude of pitching motion
k	Reduced frequency
t	Non-dimensional time
c_r	Non-dimensional root chord
C_L	Lift coefficient
C_D	Drag coefficient
C_M	Pitching moment coefficient

Chapter 1

Introduction

Wind tunnels are used to test the aerodynamic characteristics of aircraft in the research and development stages. However, the influence of the tunnel walls must be taken into account when considering test results. Historically, wind tunnel corrections have been based on Linear Potential Flow Theory [1]. In order to obtain good quality and reliable test data, factors relating to wall interference, flow angularity, local variations in velocity, and support interference, etc., must be taken into account. Karou [2] found that for delta wings with Aspect Ratio equal to one, which spanned up to half the tunnel width, classical wall correction techniques can be used to correct flow field and force results, up to 30^o angle of attack. Also, for swept wings with a blockage ratio (ratio of model planform area to tunnel cross-sectional area) of less than 0.08, tunnel interference effects can usually be considered negligible [3].

Clearly, the flow conditions within a wind tunnel will be different to those a wing would experience in free air. The interactions between the wing and wall flow fields induce longitudinal and lateral variations (streamline curvature and aerodynamic twist respectively) to the freestream, in addition to those attributed to the wing alone. These differences may result in a reduction in the average downwash experienced by the model, in a change in the streamline curvature about the model, in an alteration to the local angle of attack along the span of the model, in a change in dynamic pressure about the model due to solid and wake blockage, and in the buoyancy effect due to the axial pressure gradient along the tunnel test section. The magnitude of these effects will increase with model size (increasing solid blockage).

Previous investigations have been performed on static wings inside various tunnels. Generally the focus of these studies has been to ascertain a method to correct force data through various methods. Frink [4] looked at variations in streamline curvature and aerodynamic twist due to the presence of the tunnels walls. He also found that the tunnel walls increased the suction peak on the wing beneath the leading edge vortices. This increased suction was put down to the upflow variation increasing the mean angle of attack.

Thomas and Lan [5] used a thin layer Navier-Stokes solver to compute the flow field around a wing inside the NASA Langley Basic Aerodynamics Research Tunnel (BART). Using the wall pressure signatures obtained from the Navier-Stokes simulations as a boundary condition for an Euler simulation, they used a wall pressure signature type method to calculate the interference flow field. Their results showed that the upwash along the chord of the wing increased towards the trailing edge. Hsing and Lan [6] used a similar method to derive correction charts. Their results

also showed an increase in the suction peak beneath the primary vortices. Their computations of aerodynamic twist and upflow variations agreed well with those of Frink [4].

Weinberg [7] modeled the wind-tunnel walls with eight images of vortices inside the test section. Two pairs of vortices were taken into account, the separated leading edge vortices and an additional pair of vortices to model the wing's bound vorticity. The leading edge vortices were modeled using straight lines for the vortex cores, and were positioned above the wing using experimental data. The results obtained by Weinberg were compared to the more accurate results of Frink [4], and were found to be sufficiently accurate.

Weinberg's computations showed (for a 70^o swept wing at 30^o incidence) that "the induced upwash is relatively small near the wing's apex and grows larger toward the trailing edge - a fact that creates an effectively cambered wing under the influence of the test section walls". Previous experimental results have shown that a positively cambered wing (i.e. the local incidence of the trailing edge is greater than that at the apex) delays vortex breakdown travel to the apex. Based on the previous conclusions, Weinberg surmised that the effect of the induced camber caused by the presence of the wind tunnel walls, would delay vortex breakdown travel towards the apex, which is in direct contrast to the intuitive result that wall effects tend to increase angle of attack, thus promoting vortex breakdown travel towards that apex. Weinberg also conducted an experimental investigation into wall effects. He tested two sets of three wings (one set with 60^o sweep, and one set with 70^o sweep), each wing with a different span size. The experiment was performed in a square water tunnel (low Re) at a constant flow velocity of 11m/s. The tunnel size was 41cm x 41cm. He found that for the three wings with 70^o sweep, as the wing size was increased (kept at a constant angle of attack), vortex breakdown moved downstream. For the three wings with 60^o sweep, he found that as the wing span-to-tunnel width ratio increased from 0.175 to 0.35, the wall effects followed the computed trends (i.e. vortex breakdown was shifted downstream with increasing wing size), however, when the wing span-to-tunnel width ratio was increased from 0.35 to 0.7, no significant change was observed. This suggested that effective camber was not the only influence the wind tunnel walls had on the flow. For both the 60^o and the 70^o wings, the difference in breakdown location observed from the smallest model to the largest model, was of the order $25\%c_r$.

Thompson and Nelson [8] investigated experimentally the influence tunnel walls had on a 70^o delta wing by testing a full scale, two thirds scale, and a half scale model in a square tunnel (the largest model gave the ratios S/H = S/W = 0.364). Due to a steady hysteresis effect the wing was tested quasi-steadily on an upward and downward stroke. It was found that for the smallest model tested (S/H = S/W = 0.124) the breakdown location shifted downstream by as much as $15\%c_r$ on both the quasi-steady upstroke and downstroke. For the half scale model and the full scale model, there appeared to be little difference in the breakdown locations. As stated by Thompson and Nelson, this shift downstream of the breakdown location as model size is decreased is in contrast to the results of Weinberg [7] who found that decreasing the model size shifted the breakdown location upstream. It was noted that Weinberg used a Reynolds number an order of magnitude lower, and that Weinberg kept the velocity constant as opposed to keeping Re constant (as did Thompson and Nelson). It was observed that the vortex suction on the model surface increased with model size.

Thompson and Nelson also conducted some unsteady experiments, varying the angle of attack from 0^o to 60^o. They found that the unsteady variation in breakdown location was unaffected regardless of wing size. A similar effect was stated to have occurred with a higher frequency of oscillation.

Chapter 2

The Euler Equations

2.1 Assumptions

The general assumptions for Euler flows are as follows :

- The flow is inviscid
- The flow is adiabatic
- The flow can be incompressible or compressible

Since viscosity is neglected no boundary layer can be predicted in Euler simulations. As a result separation will not occur unless in special circumstances. It should be noted however, that if separation does occur at the leading edge of a delta wing, the Euler equations can correctly describe the transport of vorticity and entropy from the the leading edge, along the vortex sheet, to the roll up into the leading edge vortices.

2.2 Crocco's Theorem

Crocco's Theorem relates entropy gradients to vorticity in frictionless, non-conducting, steady, adiabatic flows. In natural coordinates Crocco's theorem [9] can be written as follows,

$$T\frac{dS}{d\mathbf{n}} = \frac{dh_0}{d\mathbf{n}} + u\omega$$

Simply put, Crocco's theorem states that zero vorticity implies uniform entropy, provided the stagnation enthalpy is constant. Since the stagnation enthalpy is constant in most aerodynamic problems ($h_0 =$ const. for a perfect gas), for vorticity to be generated in an inviscid flow, entropy layers must be present. In the case of Euler flows where the flow is isentropic, adiabatic, and inviscid, vorticity cannot be generated (in accordance with Kelvin's Laws). However, one source of entropy gradients in inviscid flows is the entropy rise across a shock wave since entropy is constant along streamlines unless that streamline passes through a shock.

2.3 Numerical Issues

All numerical schemes have some sort of numerical dissipation associated with them due to the discretisation of the domain. The dissipative terms are also known as artificial viscosity and are especially important in regions with high flow gradients. As such, for flow around sharp leading edges (such as those on delta wings) where flow gradients are likely to be high, there will be a significant amount of numerical dissipation, especially if the region is not adequately resolved. This numerical dissipation serves to increase the entropy (or decrease the total pressure) of the flow, and will allow the generation of vorticity in Euler solutions.

For wings with rounded leading edges, interpretation of separated flow results requires more caution since the separation location is not fixed (as with sharp leading edges). The total pressure losses (or entropy gradients) due to numerical dissipation depend on the flow gradients, grid density and numerical algorithms.

Chapter 3

Test Cases

Computations have been performed on the WEAG-TA15 wing (figure 8.1). The model consisted of the half wing alone (no body, stings, mountings etc.) inside a square tunnel, a 3x2 tunnel, and a 2x3 tunnel (tunnel details given in table below). The frontal area blockages for each tunnel were 6.69% for the 2x3 and 3x2 tunnels, and 4.2% for the square tunnel. The WEAG-TA15 wing has been used in previous unsteady Euler simulations [10][11], and these studies have provided a strong foundation for this research.

TUNNEL	S/W	S/H	M	k
SQUARE	0.42	0.42	0.4	0.56, 1.5
3 X 2	0.42	0.63	0.4	0.56, 1.5
2 X 3	0.63	0.42	0.4	0.56, 1.5

In order to be able to perform a fair comparison between different tunnels, it was decided that one mesh should be constructed in such a way that removing blocks would allow different tunnel shapes to be assessed. The topology that facilitated this with relative ease was the H-H topology. The tunnel grids generated are shown in figure 8.3.

There were 320 blocks in the "farfield" mesh with 1,770,000 grid points. This mesh had the farfield boundary condition applied at 20 c_r lengths from the wing in all directions. Extracting blocks from the farfield mesh gave the different tunnel grids. The square tunnel grid consisted of 80 blocks with 923,000 grid points, the 3x2 tunnel grid consisted of 40 blocks with 801,000 grid points, and the 2x3 tunnel grid consisted of 56 blocks with 811,000 grid points. All three tunnel grids had the farfield condition specified at the inlet and outlet, 20 c_r lengths from the wing, and the wing was meshed at 21^o. Initial cell spacing near the leading edge was $0.002c_r$ (shown in figure 8.2).

All simulations were performed using PMB3D [12], which was developed in the Dept. of Aerospace Engineering, University of Glasgow. All computations were inviscid, at a Mach Number of 0.4 (to eliminate the need for low Mach number preconditioning), with a pitching amplitude of 6^o, and reduced frequencies of motion of 0.56 and 1.5. The wing was meshed inside the tunnels at the mean incidence (α_m) of -21^o. The forcing function used was :

$$\alpha(t) = \alpha_m + \alpha_0 sin(2kt)$$

There were 50 time steps per cycle and computations were run until the removal of transient effects (this is usually achieved after 4 complete cycles). A solution (not yet periodic) for the pitching wing inside the 3x2 tunnel, at the highest reduced pitching frequency of 1.5, using 100 time steps per cycle, is shown in figure 8.4. As can be seen 50 time steps provides an adequate temporal resolution of the motion. It should be noted that the frequency of the helical motion of the vortices that is associated with the frequency of vortex breakdown, is too high to be resolved by the present computations, even with the smaller time step.

Chapter 4

Validation

Before computations were performed on the wing inside the tunnels, simulations of the pitching delta wing were performed with farfield conditions at the outer boundaries. Figures 8.5 and 8.6 compare the computed surface pressure distributions for the steady case at 21^o angle of attack with experimentally obtained distributions [13]. Figures 8.5 and 8.6 show the pressure distributions at $30\%c_r$ and $60\%c_r$ respectively. Figure 8.5 shows that the Euler solutions predict the suction peak induced by the primary vortices, but no secondary vortices are present as expected. It can also be seen from figure 8.5 that the Euler code over-predicts the suction peaks of the primary vortices when compared to experiment, and also that the vortex core is more outboard (nearer the leading edge). This is due to the lack of secondary vortices in the Euler solution, which are well known to shift the primary vortex core inboard and off the surface. Figure 8.6 again shows the surface pressure distributions but at a more downstream location. Here the Euler suction peak is less than that of experiment indicating that vortex breakdown is occurring nearby (as seen in figure 8.7). It is therefore concluded that the Euler solutions have over-predicted the breakdown location.

Figures 8.16 and 8.17 give a comparison of the lift and drag curves from the tunnel grid Euler solutions, with the experimental data [13] for k = 0.56. The pitching motion was performed by deforming the mesh using TFI (Trans-Finite Interpolation). A feature of figures 8.16 and 8.17, is that there is a slight distortion of the hysteresis loops near 27^o incidence on the downstroke. This is due to the over-prediction of vortex breakdown in the Euler solutions, which causes the flow to become completely separated from the wing at the high incidences as the breakdown reaches the apex. A final feature of figures 8.16 and 8.17 is the narrower hysteresis loop predicted by the Euler solutions when compared to those of experiment. This suggests that the unsteadiness is less pronounced in the Euler solutions. However, figures 8.16 and 8.17 show that the Euler code is capable of predicting the unsteady characteristics of pitching delta wings, and that the deformation of the grid has little effect on the overall characteristics of the solution. Although the magnitude of the integrated forces is over predicted (when compared with experiment), it can be concluded that Euler codes should be capable of predicting qualitative wind tunnel effects.

As with all CFD computations grid sensitivity can be an issue. A previous investigation with a polar tunnel grid has highlighted the sensitivity of Euler solutions to grid density, especially when resolving the flow around the leading edge. This sensitivity has been observed by other researchers [14]. Since Euler solutions require some degree of numerical error in order to allow the flow to separate at the leading

edges, and since the amount of vorticity fed into the vortex will also be sensitive to the gradients computed at the leading edge of the wing, it is perhaps unsurprising that the solutions will be fairly grid dependent. It should be noted that while the solutions are sensitive to the grid, the overall trends remain unchanged and the solutions can therefore be useful in qualitative analyses.

All simulations converged to a log residual of -6 with the maximum residual being located at the leading edge of the wing.

Chapter 5

Results and Discussion

5.1 Steady Results

Before unsteady calculations were performed, steady calculations for each of the tunnels considered were conducted. The steady computations had the wing stationary at 21^o angle of attack. Figure 8.8 shows the steady breakdown locations for the farfield solution, and the three tunnel shapes considered. Figure 8.9 shows the steady tunnel pressure distributions, as well as the farfield pressure distribution at the closest wall locations for comparison purposes.

Considering first of all the vortex breakdown locations, it can be seen from figure 8.8 that the most noticeable shift occurs with the 2x3 tunnel, shifting the breakdown location from approximately $64.9\%c_r$ (freestream) to $55.7\%c_r$ (measuring from the apex). Not so clear is the shift occurring with the 3x2 and Square tunnels, which shift the breakdown location from approximately $64.9\%c_r$ to $63.4\%c_r$. It should be stressed that with the 3x2 and Square tunnels in particular, the shift in the breakdown location is a best estimate based on what the author considers breakdown to be (in this case, where the streaklines diverge significantly from the assumed core). The "seed points" for the streaklines were identical for all four solutions. Given that there is no significant shift in the breakdown locations when the roof and floor of the tunnel are brought closer to the wing (going from the Square tunnel to the 3x2 tunnel), it can be concluded that the most influential interference is due to the side walls. This is confirmed when we assess the effect of bringing in the side walls (the Square tunnel to the 2x3 tunnel), and observe a significant promotion of vortex breakdown. The steady breakdown locations are summarised below.

TUNNEL	S/W	S/H	Breakdown Location
FARFIELD	-	-	$64.9\%c_r$
SQUARE	0.42	0.42	$63.4\%c_r$
3 X 2	0.42	0.63	$63.4\%c_r$
2 X 3	0.63	0.42	$55.7\%c_r$

If we now consider the pressure distributions on the walls (figure 8.9) for each of the steady solutions, we can see that there are quite significant differences in the tunnel pressure distributions when compared with similar locations from the farfield

solution. The farfield pressure distributions were obtained by extracting slices at z/c_r = -0.63, and $y/c_r = \pm 0.63$. These locations correspond to the most inner wall positions of all three tunnels. It is clear from figure 8.9 that the side walls of all the tunnels have a favourable pressure gradient in the axial direction. This is expected as the vortices become closer to the side wall as they extend towards the trailing edge of the wing. Near the trailing edge of the wing at the cropped tip, the side wall induced upwash will be greatest, inducing the largest suction on the wing. The pressure gradient on the wall will become more favourable as the side wall becomes closer to the wing, which is seen as we move from the Square tunnel to the 2x3 tunnel. Another feature of the wall pressure distributions, on the 2x3 tunnel side wall in particular, is the presence of a clear vortical flow pattern on the side wall downstream of the wing's trailing edge. It is well known from experiment that the strong rotational flow extends down the tunnel, even though the vortex may have burst over the wing. This vortical flow pattern (which extends $20c_r$ lengths down the tunnel, requiring the farfield boundary condition to be applied well away from the wing) is observed for the three tunnels, reducing in extent with decreasing S/W ratio [6]. Figure 8.10 shows clearly the increasing favourable pressure gradients produced within the tunnels due to the side walls. It should be noted that all curves were extracted at the 2x3 tunnel side wall location ($z/c_r \simeq -0.625$), at the mid-line between the roof and floor. The effect of tunnel blockage can be seen in the curves at the $x/c_r = 0$, where the C_P is greater than that of the farfield solution for all tunnels. It is clear that the 2x3 tunnel produces the most blockage, and that the close proximity of the 2x3 tunnel side wall produces the largest favourable pressure gradient, and therefore, interference.

Figure 8.11 shows the pressure distribution along the centreline of the tunnels and the farfield solution. The change from the pressure side of the wing to the suction side is clearly seen near $x/c_r = 0.5625$. It is clear that the 2x3 tunnel produces the greatest blockage (seen previously in figure 8.10), as the static pressure is clearly increased upstream of the wing (implying lower dynamic pressure). This blockage reduces slightly in the 3x2 tunnel, and even further in the square tunnel. Interestingly, downstream of the wing the static pressure at the centreline is considerably lower in the 2x3 tunnel when compared to the other solutions. This is due to the fact that the highly rotational flow downstream of the wing is deflected upwards by the wall induced velocity components (considering the method of images). This upwards deflection of the rotational wake flow can be clearly seen in figure 8.9(c), and reduces with decreasing S/W ratio. Comparing the blockage from the 3x2 and 2x3 tunnels which is near equal upstream of the wing, it would appear that tunnel blockage is not the major influence promoting vortex breakdown.

Figure 8.12 shows the steady pressure distribution beneath the vortex core line on the surface of the wing. It is clear that with the 2x3 tunnel there is the largest increase in suction due to the tunnel walls. There are slight increases in suction with the Square and 3x2 tunnels, however, this increase is not to the same extent as with the 2x3 tunnel. This increase in suction beneath the vortex core due to tunnel walls was observed experimentally by Thompson and Nelson [8]. Thompson and Nelson found that as S/W ratio was increased, the suction peak beneath the vortex core also increased. This increased suction has the effect of increasing the adverse pressure gradient along the vortex core, thus promoting vortex breakdown as seen in figure 8.8. This result is in contrast to that obtained by Weinberg [7], and in the descriptions of tunnel induced wall interference (based on Weinberg's results) given by Ericsson and Beyers [15][16], where breakdown was noticed to shift downstream with increasing wing size. Weinberg tested at low Reynolds number

(of the order $Re \simeq 26,000$ for his largest 60^o wing at a flow velocity of 11m/s) and found that increasing wing size caused the breakdown location to shift downstream. The explanation given was an induced camber effect, with no reference to tunnel boundary layers, volumetric blockage, incidence effects etc. Interestingly, at higher Reynolds number, Thompson and Nelson [8] noticed the opposite trend, i.e. breakdown shifted forward with increasing model size. Thompson and Nelson tested a 70^o delta wing at various incidences on both the quasi-steady upstroke and downstroke in the incidence range of 15^o to 35^o. The S/W ratios of 0.25, 0.33, and 0.5 were considered, giving frontal area blockages at 21^o angle of attack of 1.52%, 2.71%, and 6.12% respectively. The Reynolds number was held constant at 150,000 and 250,000.

The helix angles of the vortices in each of the tunnels, and in the farfield solutions were examined to see if any noticeable difference was observed. It was concluded that there was no tightening or relaxing of the helix angle of the vortex, therefore a change in the rotational characteristics of the vortex was not influencing vortex breakdown.

Figure 8.13 shows the flow incidences in all tunnels at the spanwise location of $z/c_r \simeq -0.63$, the location of the 2x3 tunnel side wall. It is clear that, as expected, the proximity of the side wall induces the highest upflow when compared to that of the Square and 3x2 tunnels. It is also clear that the mean incidence the wing experiences in the 2x3 tunnel is much higher than that of the wing in the Square and 3x2 tunnels. This explains the suction peak increases seen in figure 8.12 as the wing is placed in the various tunnels. It is also clear that the 2x3 tunnel will produce the greatest induced camber, since the induced upwash (subtracting the farfield solution incidences from the tunnel solution incidences) clearly rises the quickest in the 2x3 tunnel. Weinberg [7] stated that this induced camber effect will delay vortex breakdown in accordance with the experiments of Lambourne and Bryer [17], however it is clear from the measured breakdown locations in the tunnel solutions, that the higher mean incidence effect is the dominant influence on the vortex breakdown. It is quite possible that the induced camber effect could be dominant at low Reynolds number and low flow velocity. Infact for the 60^o delta wing Weinberg tested, he found that increasing the S/W ratio from 0.175 to 0.35 (changing the frontal area blockage from 0.48% to 1.91%) caused breakdown to shift towards the trailing edge, however, increasing the S/W ratio from 0.35 to 0.7 (changing the frontal area blockage from 1.91% to 7.65%) produced no further effect on the breakdown location. This indicated that induced camber was not the only effect present.

Figures 8.14 and 8.15 show the surface pressure distributions from the four solutions at $30\%c_r$ and $60\%c_r$ respectively. At the $30\%c_r$ location, it can be seen that the 2x3 tunnel induces the highest suction peak, and also shifts the vortex core inboards the furthest. This can be attributed to the side wall effect if we consider the method of images, where the wall induces an additional upward velocity component on the flow at the wall. This will shift the vortex core upwards and inwards. This increase in the suction peak was observed in previous investigations [8][6]. At the $60\%c_r$ location it is clear that the vortex in the 2x3 tunnel is almost completely burst, while the others are nearing breakdown.

5.2 Unsteady Results

Unsteady pitching calculations were performed at two reduced frequencies, k = 0.56 (experimental reduced frequency), and k = 1.5 (artificially large pitching frequency).

The lift and drag curves for the k = 0.56 case are shown in figures 8.16 and 8.17, and the lift and drag curves for the k = 1.5 case are shown in figures 8.18 and 8.19. Figures 8.20 to 8.27 show the unsteady breakdown locations for both reduced pitching frequencies, and for all farfield and tunnel grids.

As mentioned previously, for the lower reduced frequency of k = 0.56 with farfield conditions at the outer boundaries, there appears to be a deformation of the hysteresis loop around 27^o angle of attack. This can be attributed to the fact that vortex breakdown has reached near the apex of the wing, as seen in figure 8.20(h). This is again seen for the same incidence in each of the tunnels, figures 8.22(h), 8.24(h), and 8.26(h). Interestingly, with the higher reduced frequency of k = 1.5, vortex breakdown never gets close to the apex (figures 8.21, 8.23, 8.25, and 8.27), leading to the smooth hysteresis loops shown in figures 8.18 and 8.19. It is also clear from figures 8.20 and 8.21, that an increase in reduced frequency leads to an increase in the phase lag of the breakdown motion [18].

Figures 8.28 and 8.29 summarise the vortex breakdown locations taken from figures 8.20 to 8.27. It should be noted that the breakdown locations have been taken as the point where the streaklines diverge significantly from the assumed vortex core. In the absence of a precise universal definition of vortex breakdown, this method offers consistency and should allow different trends to be highlighted. The locations given are therefore the author's interpretation of the breakdown position, and should only be considered as a means of identifying trends as opposed to exact locations. It is clear from figures 8.28 and 8.29 that the 2x3 tunnel varies the breakdown locations the most (as in the steady case). Figures 8.28 and 8.29 also show that for both the frequencies considered, the Square and 3x2 tunnels tend to produce similar breakdown locations, which are generally slightly promoted in comparison to the farfield breakdown locations. It can therefore be concluded that bringing in the roof and floor has little influence on the breakdown location, indicating that roof and floor proximity is not a dominant factor in these unsteady flows. This is in contrast to the effect of bringing in the side walls. Comparing the Square and 2x3 tunnel solutions, there is clearly a large variation in the breakdown location as the side walls become closer to the wing. This is again an indication that side wall proximity is the most dominant factor in tunnel wall interference on Delta Wing aerodynamics.

If we look closely at figure 8.28, i.e. the breakdown locations for the lower frequency pitching motion, we see that the largest deviation of the breakdown location from that obtained in freestream conditions, occurs after the vortex has burst and is reforming (on the downstroke). This is a consistent result from all three tunnels. In order to visualise the extent of the tunnel interference, figures 8.31 to 8.36 show the tunnel wall pressure distributions at the same points around the cycle. As can be seen from figures 8.31, 8.33, and 8.35, as the wing pitches down, it moves from a state with high tunnel interference (high incidence implies stronger vortices, vortex burst moving towards the apex, high blockage) to a state with lower tunnel interference, therefore we would expect the tunnel influence to be most prominent as the vortex reforms. It should be noted that despite the fact that the vortex burst is reaching the apex at high incidences, there is still strong rotational flow present as the flow negotiates the wing. Therefore despite the fact that the core of the vortex has broken down, there is still a high tunnel interference effect at high incidences, due high tunnel blockages and this highly rotational flow. Figure 8.30 shows the difference in the pressure gradient along the vortex core between solutions from freestream conditions and the 2x3 tunnel, for 15^o angle of attack. It is clear from figure 8.30 that there is a larger adverse pressure gradient caused by the 2x3

tunnel side walls even at this low angle of attack, which is a result of the high tunnel influences previously exhibited on the flow. As the breakdown begins to move back towards the apex (i.e with increasing incidence), the wing is leaving a state of low tunnel interference (figures 8.35(c,d)) and therefore we would expect tunnel influences to be less important on the upstroke (as seen in figure 8.28). A final noticeable difference between the breakdown curves from the 2x3 tunnel and the farfield solutions, is the rate at which breakdown begins to shift back from the apex. Comparing the gradients of the curves from 21^o to 16.9^o (when the vortex starts to significantly reform), we see that the breakdown shifts downstream at a lower rate in the 2x3 tunnel when compared with the farfield solution. Again this is due to the fact that the tunnel influence is highest after the wing has reached its maximum incidence (figures 8.35(g,h)), and the vortex has completely burst (the tunnel influence on the vortex can be expected to be highest after the vortex has burst, due to the time lag of the vortex breakdown response to external influences). Also, it is clear that tunnel influences aren't very important when the vortex is completely burst, only when the vortices are trying to reform. Therefore there is an expected slow down in the motion of the breakdown as the vortex recovers. When the vortex recovers and is at its weakest at the lower incidences, and when the tunnel interference is lowest due to the lower incidence, the motion of the breakdown becomes similar to that of the freestream which is indicated by similar gradients of the breakdown motion in the range of 21^o upwards.

If we now look at figure 8.29, i.e. the breakdown locations for the higher frequency pitching motion, it is clear that the breakdown motion is out of phase with the motion of the wing by a considerable amount. From 25^o on the upstroke to 16.9^o on the downstroke we see that the breakdown moves upstream towards the apex, becoming closest to the apex at 16.9^o angle of attack. As with the lower reduced frequency pitching motion, the tunnel interference is highest at the high angles of attack, where high blockage is present. Unlike the lower frequency pitching motion, the vortex breakdown is near the trailing edge at high incidence, and is beginning to move upstream. Therefore once again we have the wing moving from high tunnel interference (figures 8.36(f,g,h)) to lower interference as the wing pitches down, therefore the rate at which vortex breakdown shifts upstream towards the apex is increased, and the difference between the breakdown locations from the 2x3 tunnel and farfield solutions becomes largest on the downstroke. Looking at the lower incidences (around 16.9^o) when the vortex recovery is just starting to take place, we see that the breakdown motion begins to recover at a higher rate than that of the freestream. Eventually this increased rate levels off and breakdown motion towards the trailing edge slows down as the tunnel influence begins to increase with incidence (16.9^o to 25.1^o). This is due to the fact that the tunnel interference is low at the low incidences (as seen in figures 8.36(b,c,d)), and therefore the breakdown location begins to move closer to that of the freestream. However, as with the lower reduced frequency case, breakdown is consistently promoted inside the 2x3 tunnel.

Chapter 6

Conclusions

A study has been conducted to investigate the effect that wind tunnel wall constraints produce on pitching delta wing aerodynamics. It has been shown, both in this investigation and in previous investigations, that the Euler equations can adequately model the response of the primary vortices produced on delta wings at incidence. Taking into account the limitations of the Euler model, the following conclusions can be drawn from the study :

- The simulations have shown that the side walls play the dominant role in wind tunnel influences on delta wings. It is clear that the swirling flow will get closer to the wall as the vortex extends from the apex to the trailing edge. The side wall induced suctions will therefore be highest near the trailing edge, reducing towards the apex. A favourable pressure gradient at the side wall is therefore formed.

- The simulations have shown that the presence of the roof and floor has a lesser influence on vortex breakdown, than that of side walls. Bringing in the roof and floor (from the Square Tunnel to the 2x3 tunnel) does not produce a significant change in breakdown location for steady and unsteady flows. This is an indication that the roof and floor are the least influential.

- Side wall proximity tends to promote vortex breakdown. The presence of the side wall increases the suction beneath the vortex core, thus increasing the adverse pressure gradient along the core. This increased suction is due to an increase in the mean incidence of the wing, which is a result of the wall induced upwash. Although there an induced camber effect on the wing due to the vortex induced upwash, it appears that at high Reynolds number, this is not the dominant influence on the vortex. This result agrees qualitatively with the experimental results of Thompson and Nelson [8].

- The promotion of vortex breakdown is observed in both steady and unsteady computations, however, for sinusoidal pitching motion, the extent of the breakdown promotion is dependent on the reduced frequency, and whether the wing is on its upstroke or downstroke.

- Side walls have a strong effect on the rate of motion of the vortex breakdown, whether it be vortex recovery or breakdown travel towards the apex. This can be attributed to the fact that the tunnel influence will be highest at the high incidences (high frontal area blockage), and will therefore influence heavily the breakdown motion in this regime.

- The side wall influence tends to be greatest on the downstroke of the motion. This has been shown in the simulations as large deviations in the breakdown locations between the 2x3 tunnel solutions and the farfield solutions. This is due to the fact that the wing is moving from a state of high tunnel interference to low tunnel interference.

- Navier-Stokes calculations need to be performed in order to assess the viscous effects present in real life tests. It has been shown that the Euler model does not respond to the pitching unsteadiness to the same degree as experiment, therefore it is possible the inviscid vortices will not respond to tunnel influences to the same extent. Similarly the effect of tunnel influences on the secondary vortices, and how their breakdown variations effect the primary vortex breakdown must be investigated. It is expected that the trends will not vary with viscous flow, however this must be confirmed.

Chapter 7

Acknowledgements

Thanks to Dr. K. Badcock and Prof. B. E. Richards of the CFD Group, University of Glasgow for their help during the project. Thanks also go to Dr. F. Coton of the Low Speed Aerodynamics Group, University of Glasgow, for his help and useful comments on the flow physics observed in the solutions.

Chapter 8

Figures

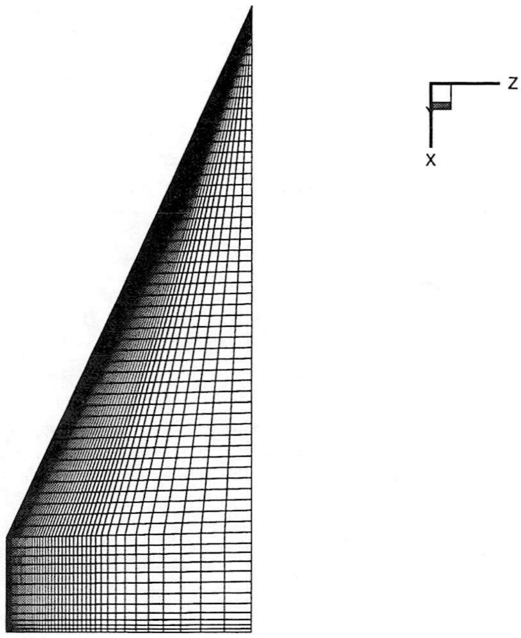

Figure 8.1: *The WEAG-TA15 Wing Surface Mesh (Symmetric in the z-plane)*

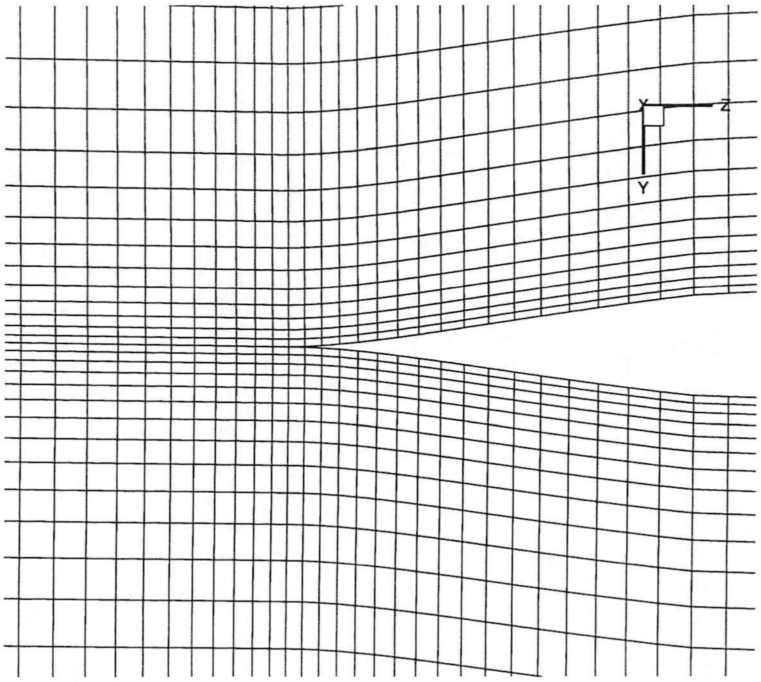

Figure 8.2: *Grid point distribution at the leading edge of the wing. Slice taken at the chordwise station 85%*c_r

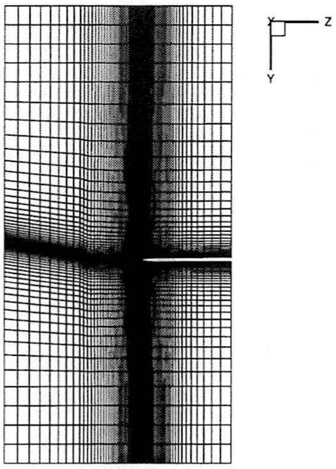

(a) Square Tunnel, S/W=0.42, S/H=0.42

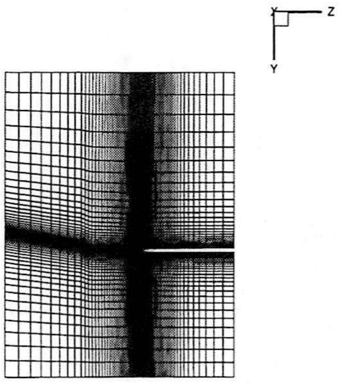

(b) 3x2 Tunnel, S/W=0.42, S/H=0.63

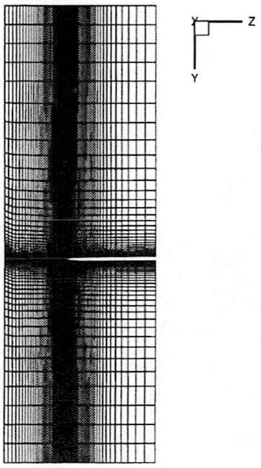

(c) 2x3 Tunnel, S/W=0.63, S/H=0.42

Figure 8.3: *Wind tunnel shapes considered in this study*

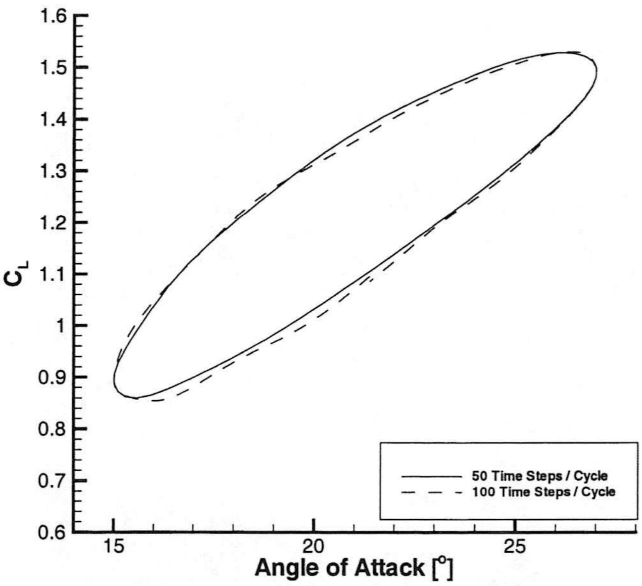

Figure 8.4: *Temporal refinement study, 2x3 tunnel, k=1.5, Unsteady flow*

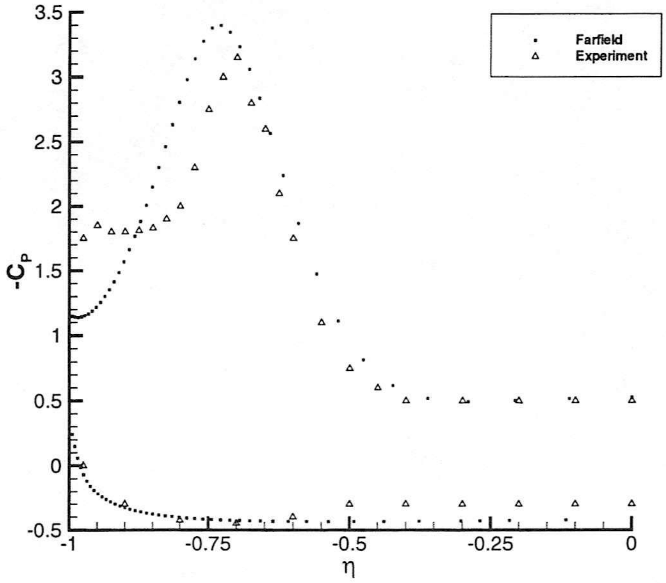

Figure 8.5: *Comparison of surface pressure distribution at 30%c_r, farfield solution with experiment,* 21^o *Angle of Attack, Steady Flow*

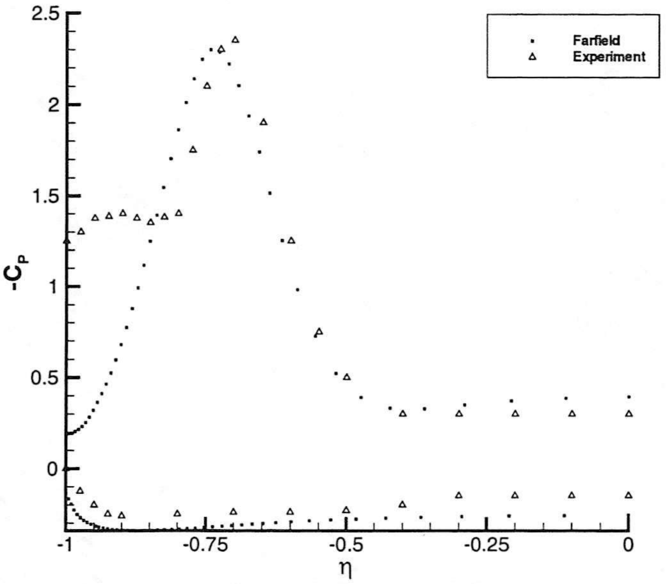

Figure 8.6: *Comparison of surface pressure distribution at 60%c_r, farfield solution with experiment,* 21^o *Angle of Attack, Steady Flow*

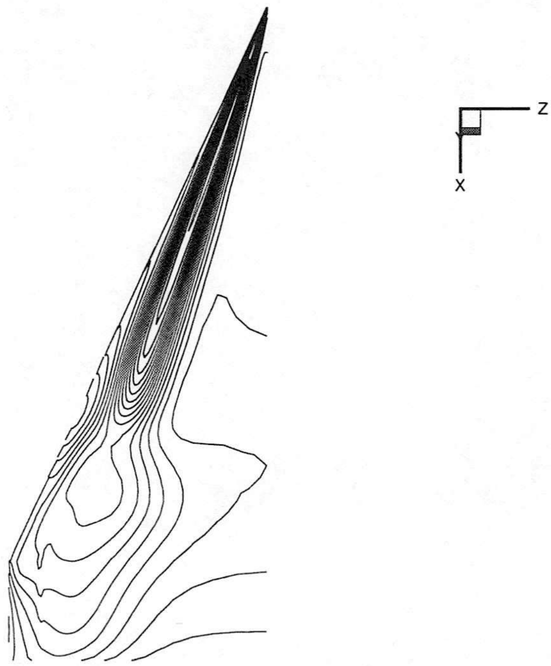

Figure 8.7: *Computed upper surface pressure distribution, farfield solution,* 21^o *Angle of Attack, Steady Flow*

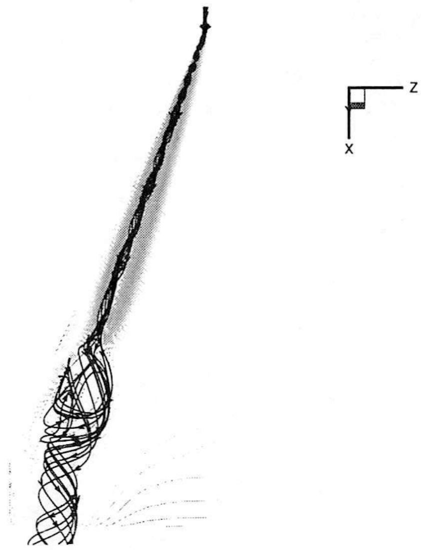

(a) Square Tunnel

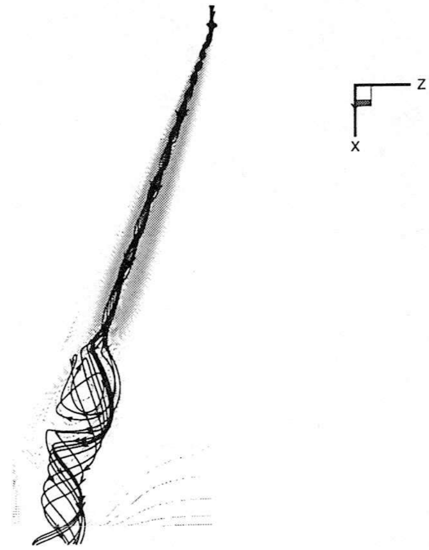

(b) 3x2 Tunnel

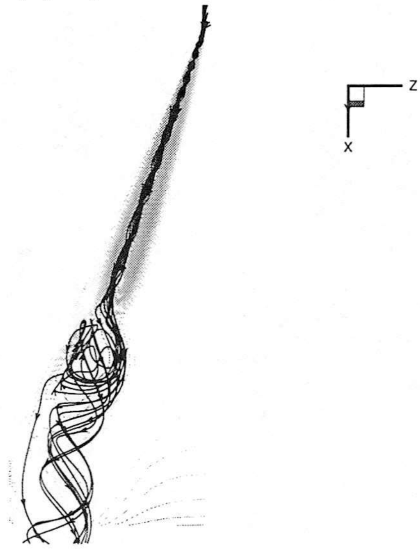

(c) 2x3 Tunnel

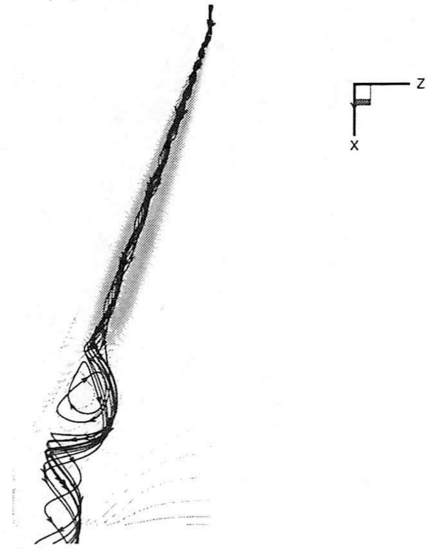

(d) farfield

Figure 8.8: *Steady flow breakdown locations, 21^o Angle of Attack, Steady Flow*

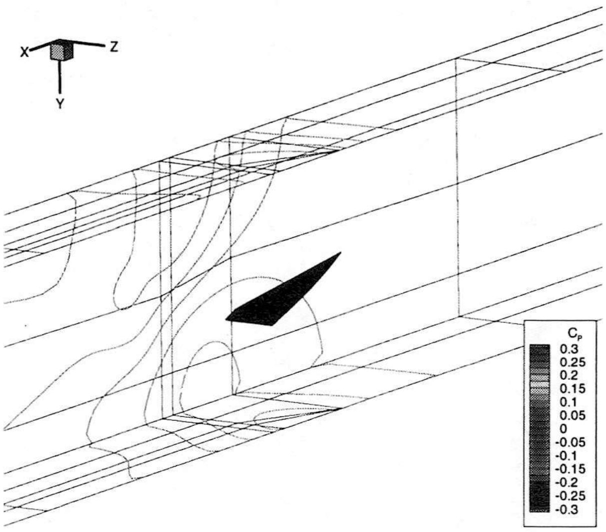

(a) Square Tunnel

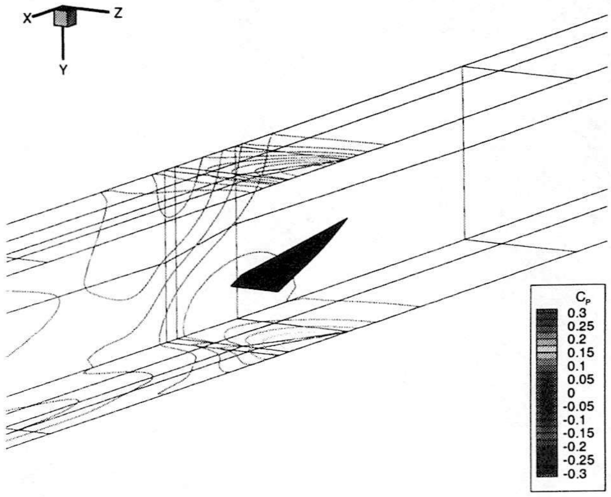

(b) 3x2 Tunnel

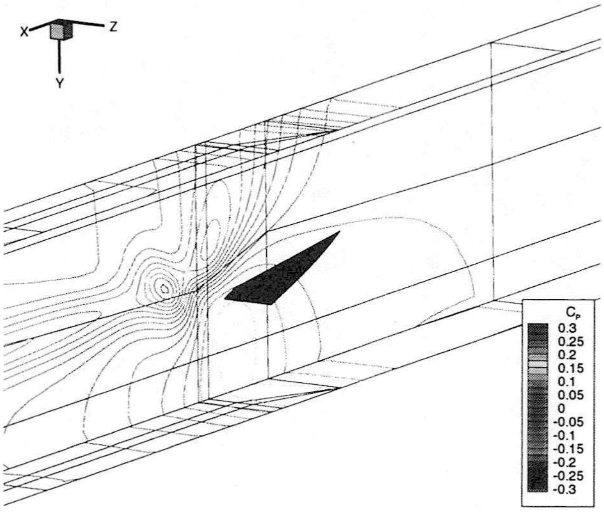

(c) 2x3 Tunnel

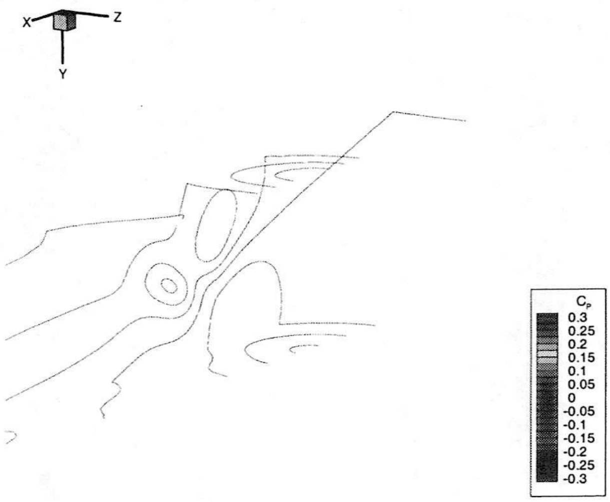

Farfield at Z = -0.63, Y = $\pm$0.63

Figure 8.9: *Steady flow tunnel wall pressure distributions, 21° Angle of Attack, Steady Flow*

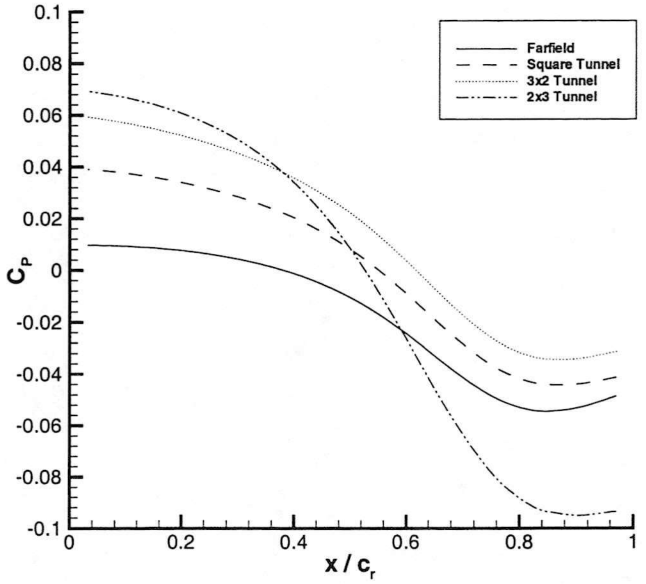

Figure 8.10: *Pressure distribution at 2x3 tunnel side wall location, on the midline between the roof and floor, 21° Angle of Attack, Steady Flow*

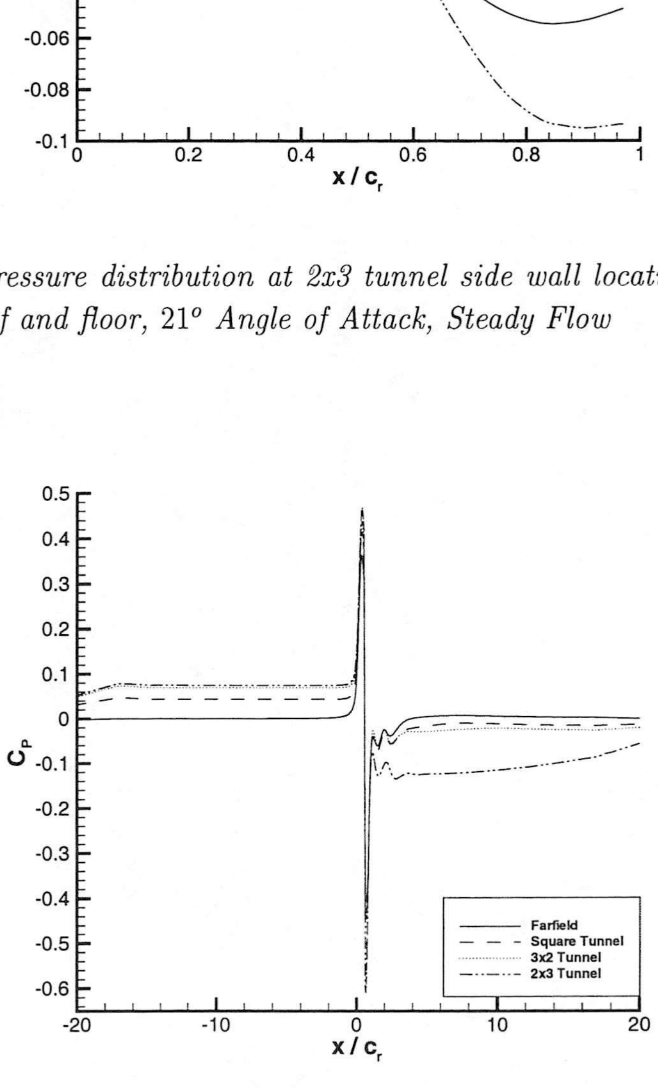

Figure 8.11: *Pressure distribution along centreline of the tunnels and farfield, 21° Angle of Attack, Steady Flow*

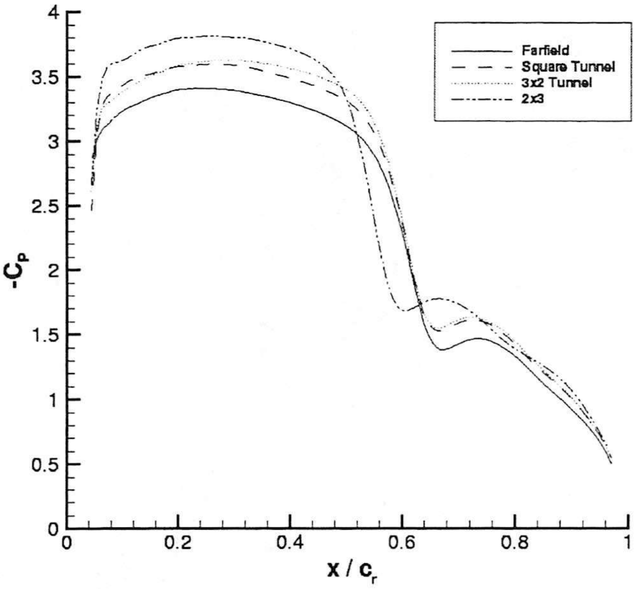

Figure 8.12: *Surface pressure distribution beneath the vortex core, tunnel and farfield solutions, 21° Angle of Attack, Steady Flow*

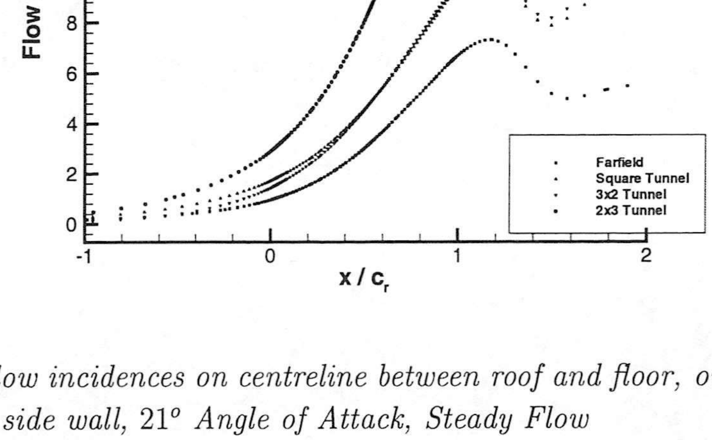

Figure 8.13: *Flow incidences on centreline between roof and floor, on the location of the 2x3 tunnel side wall, 21° Angle of Attack, Steady Flow*

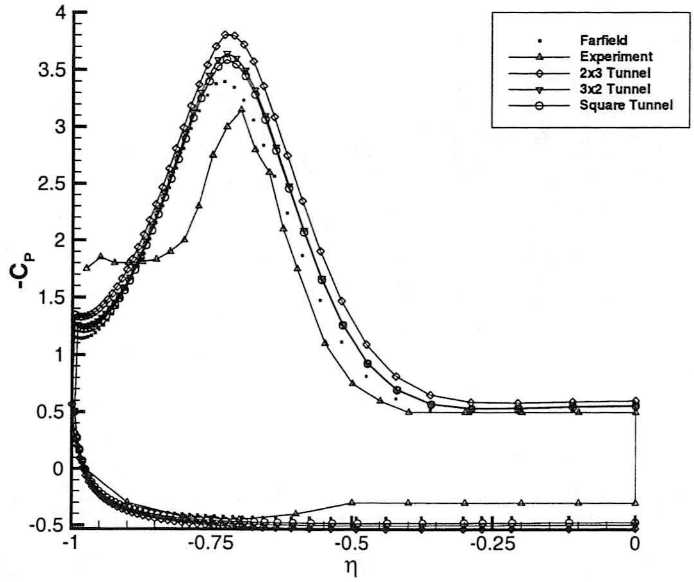

Figure 8.14: *Surface pressure distribution comparison at 30%c_r, tunnels and farfield, 21° Angle of Attack, Steady Flow*

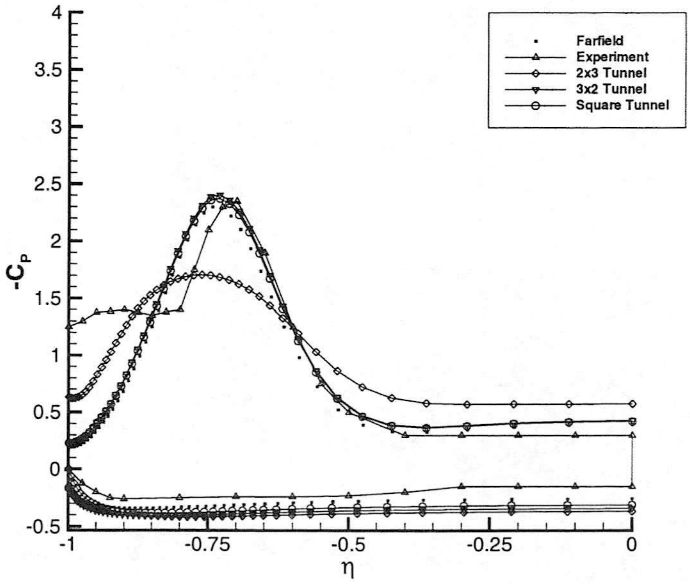

Figure 8.15: *Surface pressure distribution comparison at 60%c_r, tunnels and farfield, 21° Angle of Attack, Steady Flow*

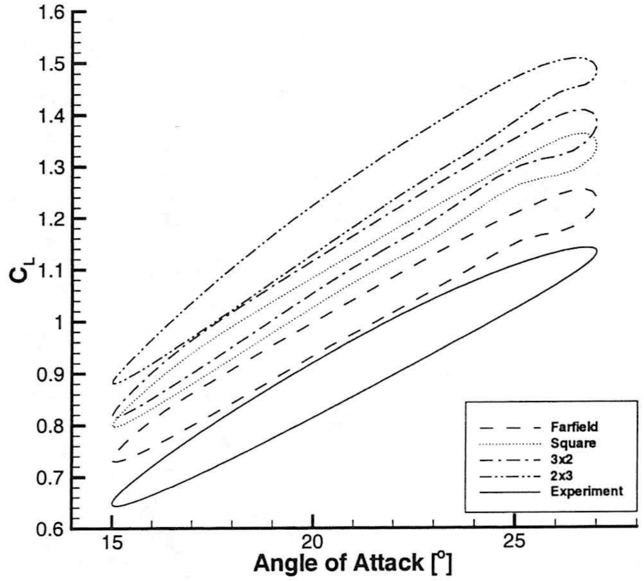

Figure 8.16: *Unsteady Lift Curves, k = 0.56*

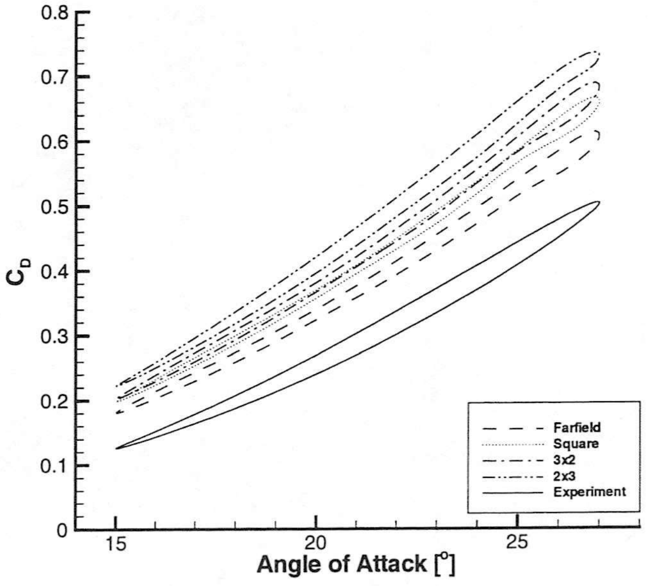

Figure 8.17: *Unsteady Drag Curves, k = 0.56*

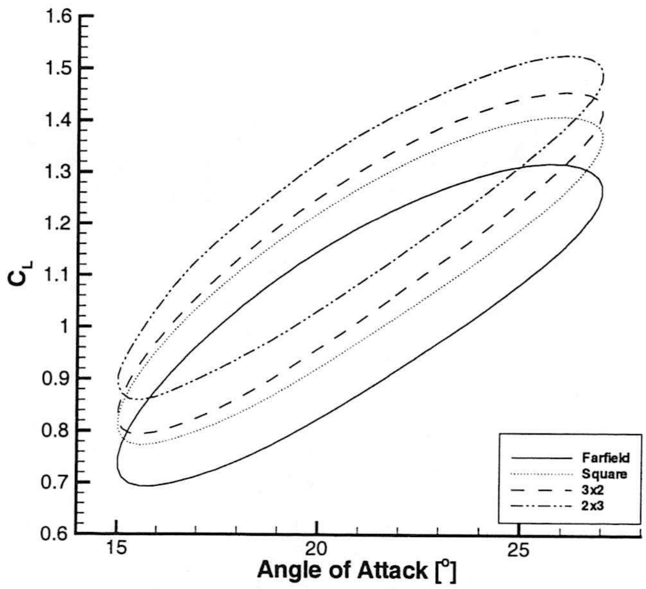

Figure 8.18: *Unsteady Lift Curves, k = 1.5*

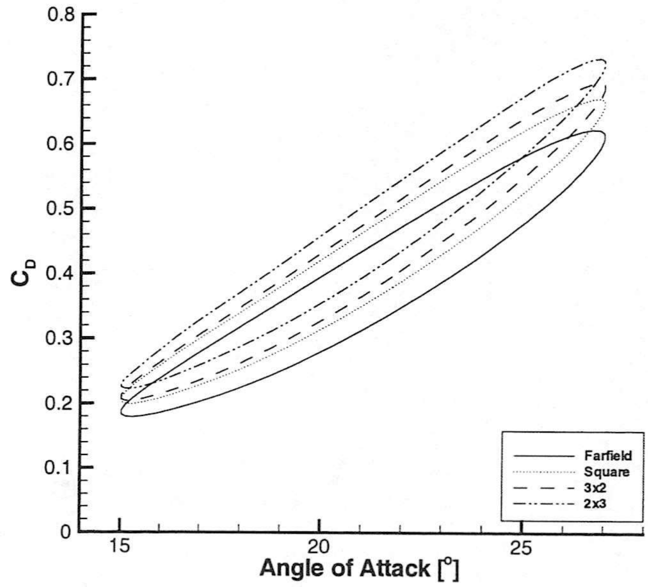

Figure 8.19: *Unsteady Drag Curves, k = 1.5*

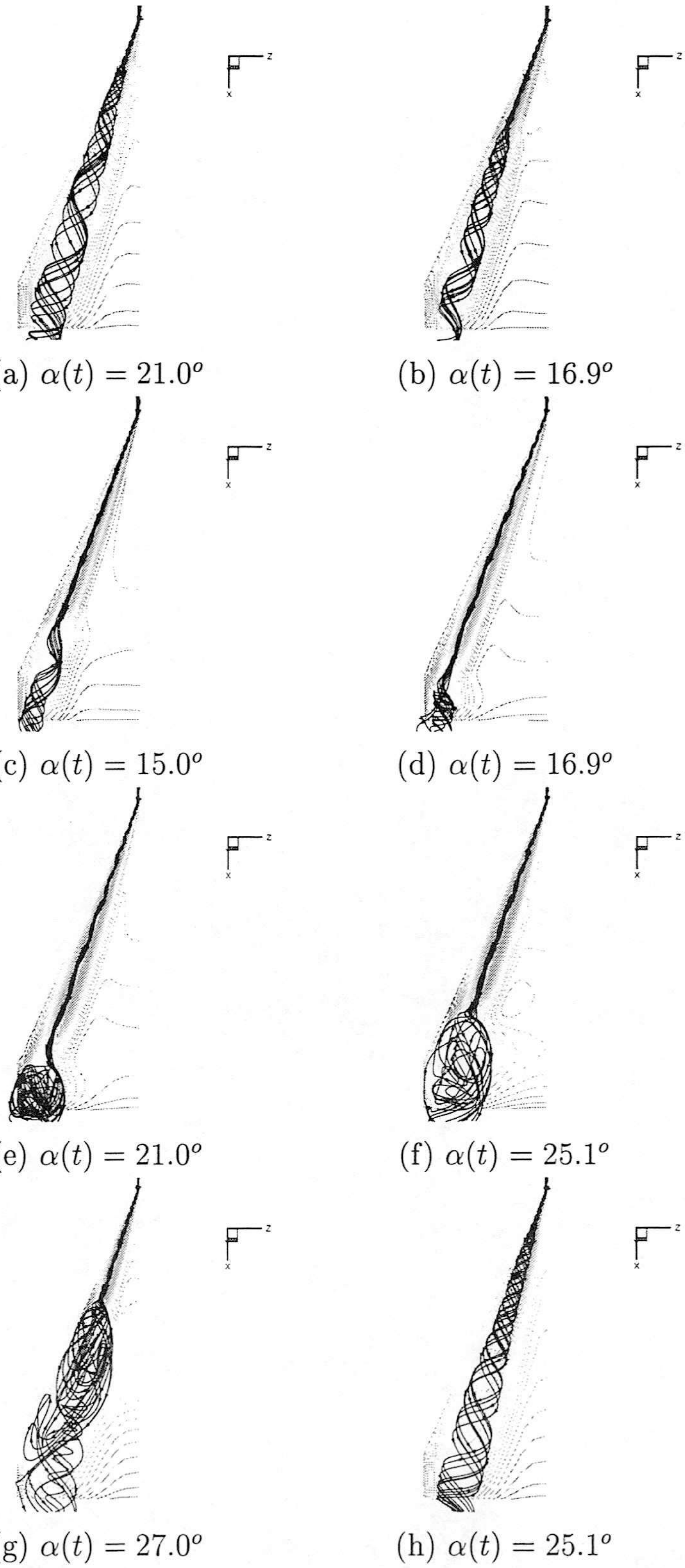

(a) $\alpha(t) = 21.0^o$ (b) $\alpha(t) = 16.9^o$

(c) $\alpha(t) = 15.0^o$ (d) $\alpha(t) = 16.9^o$

(e) $\alpha(t) = 21.0^o$ (f) $\alpha(t) = 25.1^o$

(g) $\alpha(t) = 27.0^o$ (h) $\alpha(t) = 25.1^o$

Figure 8.20: *Unsteady Breakdown Locations With Farfield Conditons at Outer Boundaries, k = 0.56*

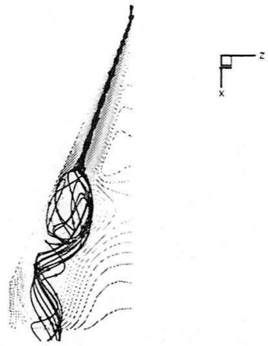

(a) $\alpha(t) = 21.0^o$

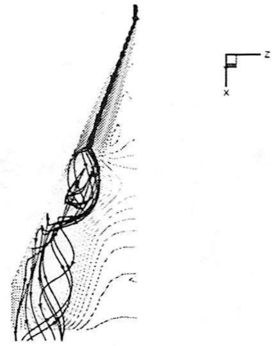

(b) $\alpha(t) = 16.9^o$

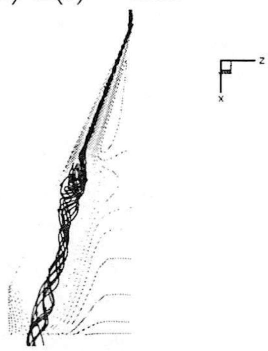

(c) $\alpha(t) = 15.0^o$

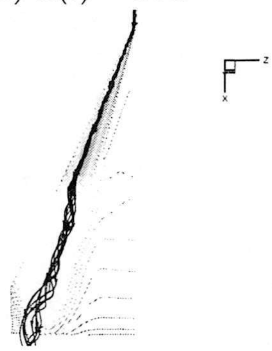

(d) $\alpha(t) = 16.9^o$

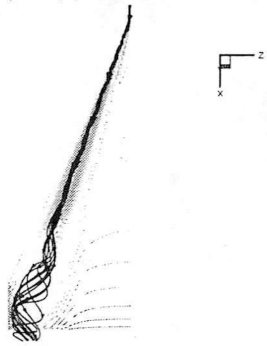

(e) $\alpha(t) = 21.0^o$

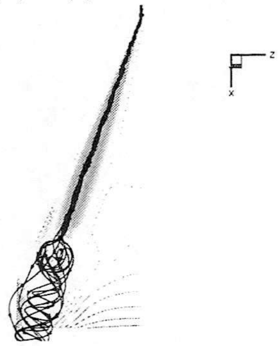

(f) $\alpha(t) = 25.1^o$

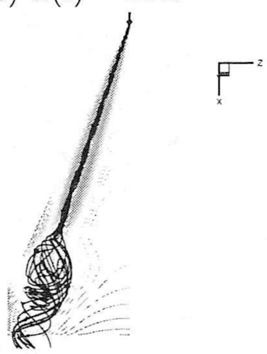

(g) $\alpha(t) = 27.0^o$

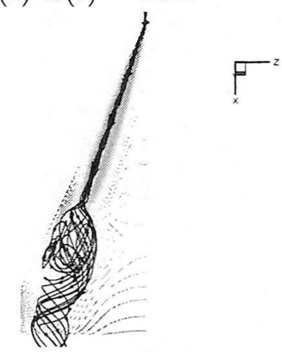

(h) $\alpha(t) = 25.1^o$

Figure 8.21: *Unsteady Breakdown Locations With Farfield Conditons at Outer Boundaries, k = 1.5*

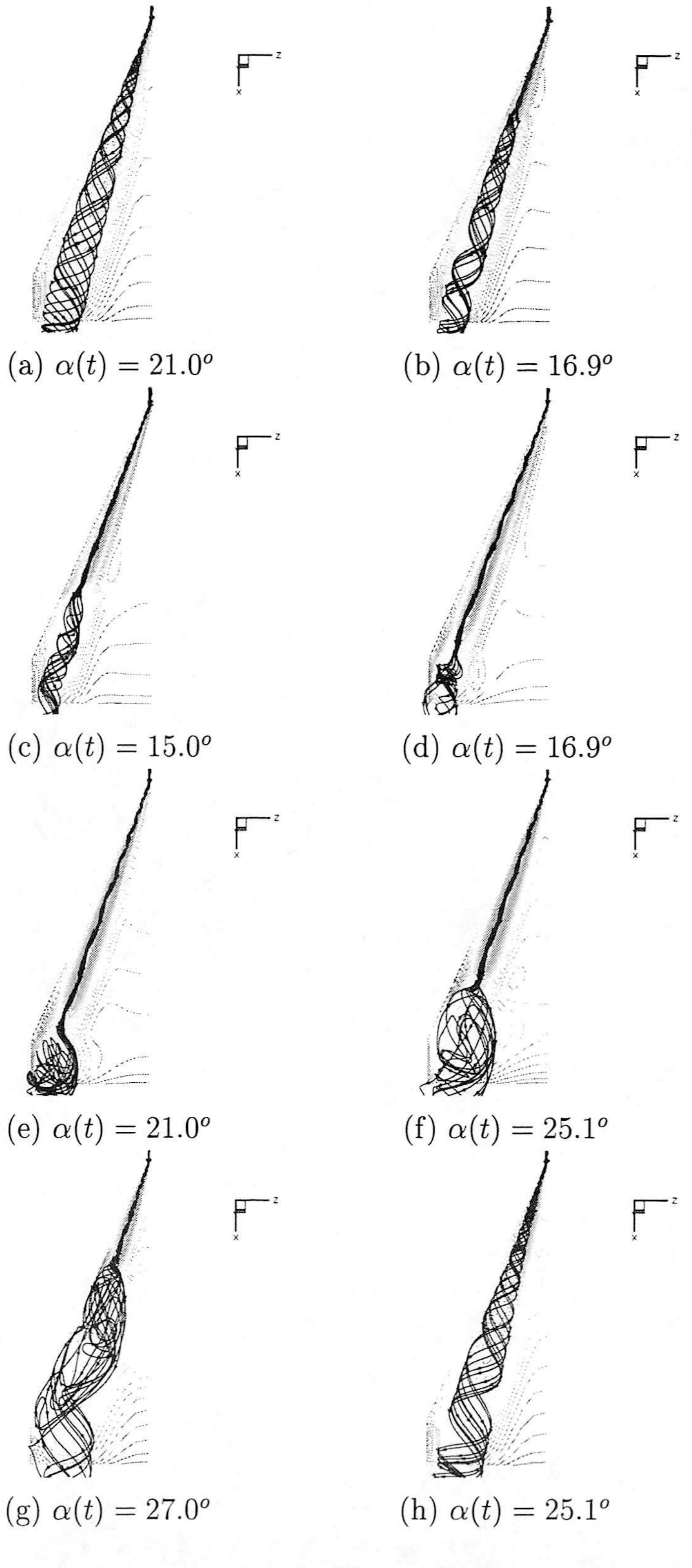

Figure 8.22: *Unsteady Breakdown Locations Within Square Tunnel, k = 0.56*

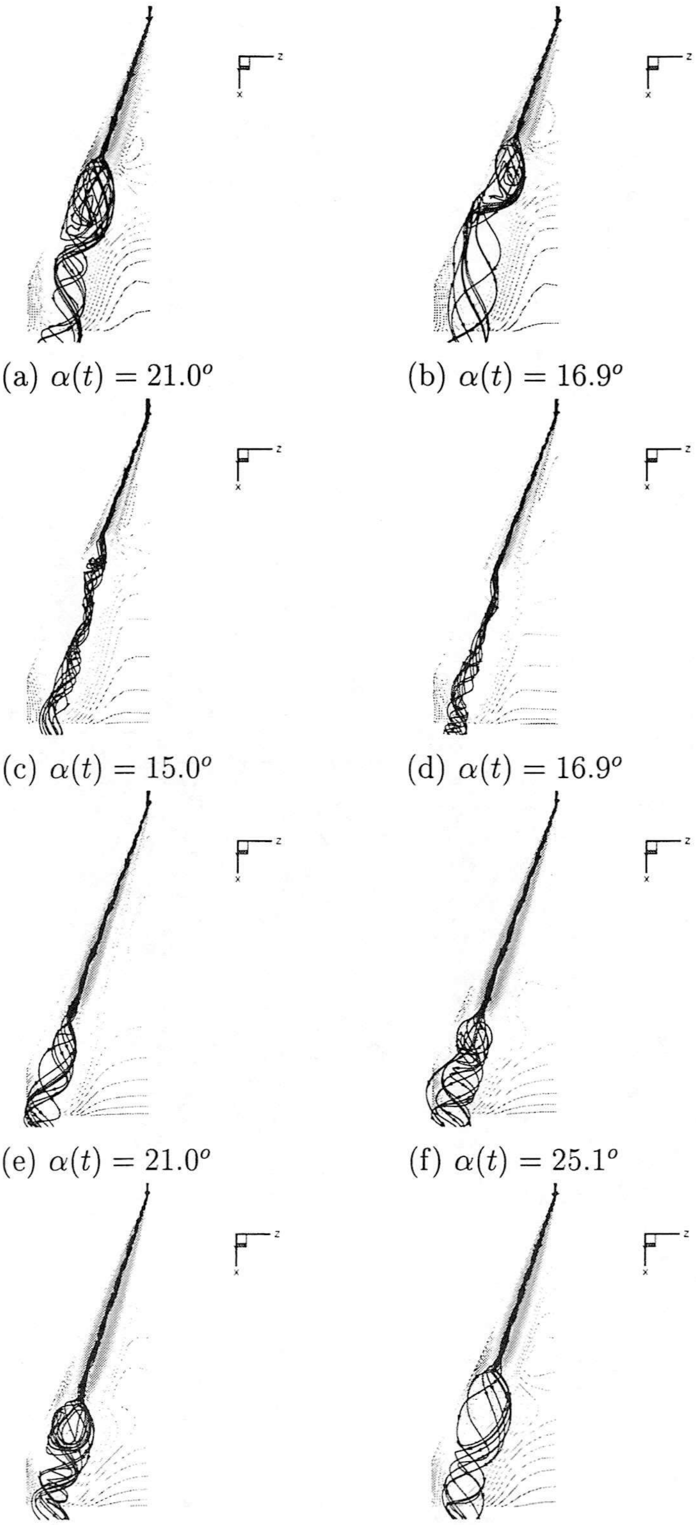

(a) $\alpha(t) = 21.0^o$ (b) $\alpha(t) = 16.9^o$

(c) $\alpha(t) = 15.0^o$ (d) $\alpha(t) = 16.9^o$

(e) $\alpha(t) = 21.0^o$ (f) $\alpha(t) = 25.1^o$

(g) $\alpha(t) = 27.0^o$ (h) $\alpha(t) = 25.1^o$

Figure 8.23: *Unsteady Breakdown Locations Within Square Tunnel, k = 1.5*

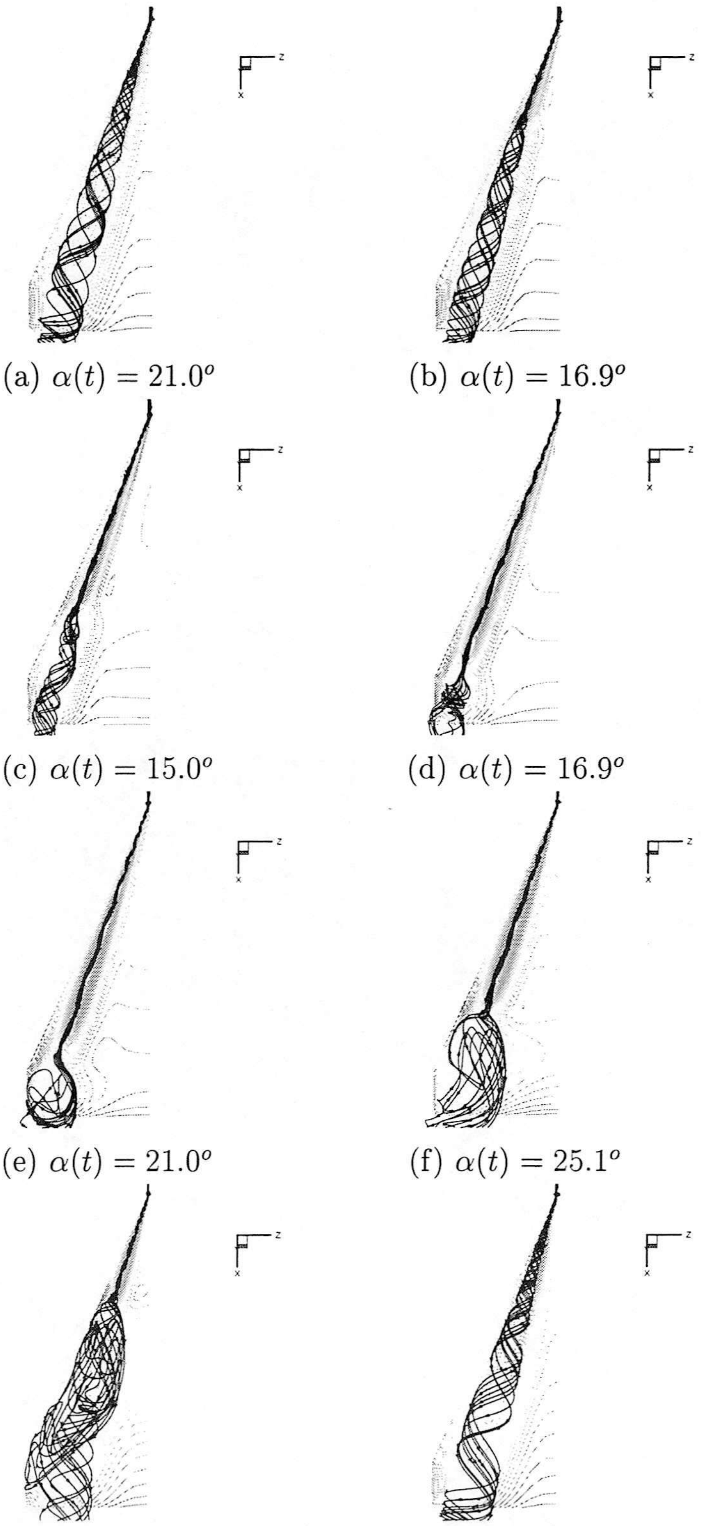

(a) $\alpha(t) = 21.0^o$ (b) $\alpha(t) = 16.9^o$

(c) $\alpha(t) = 15.0^o$ (d) $\alpha(t) = 16.9^o$

(e) $\alpha(t) = 21.0^o$ (f) $\alpha(t) = 25.1^o$

(g) $\alpha(t) = 27.0^o$ (h) $\alpha(t) = 25.1^o$

Figure 8.24: *Unsteady Breakdown Locations Within 3x2 Tunnel, k = 0.56*

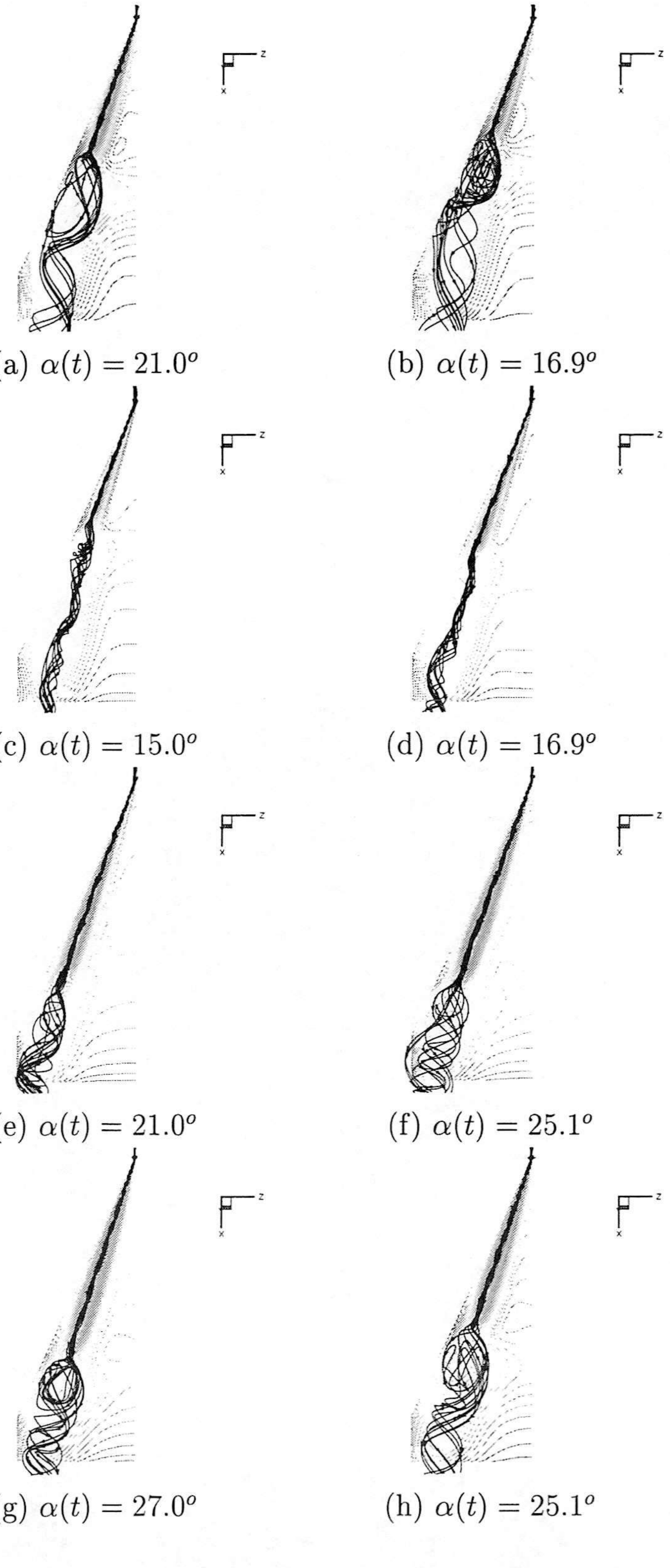

(a) $\alpha(t) = 21.0^o$ (b) $\alpha(t) = 16.9^o$

(c) $\alpha(t) = 15.0^o$ (d) $\alpha(t) = 16.9^o$

(e) $\alpha(t) = 21.0^o$ (f) $\alpha(t) = 25.1^o$

(g) $\alpha(t) = 27.0^o$ (h) $\alpha(t) = 25.1^o$

Figure 8.25: *Unsteady Breakdown Locations Within 3x2 Tunnel, k = 1.5*

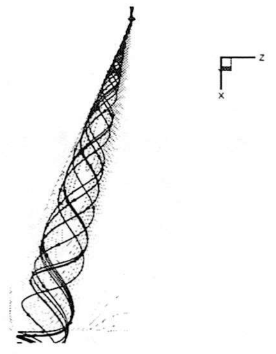

(a) $\alpha(t) = 21.0^o$

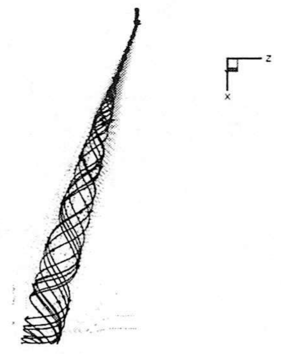

(b) $\alpha(t) = 16.9^o$

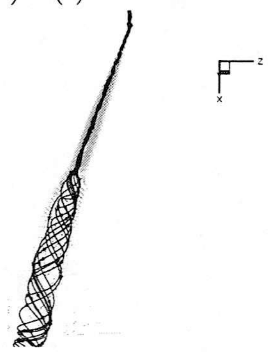

(c) $\alpha(t) = 15.0^o$

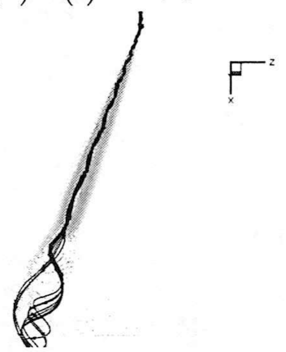

(d) $\alpha(t) = 16.9^o$

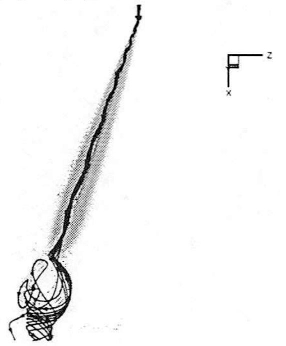

(e) $\alpha(t) = 21.0^o$

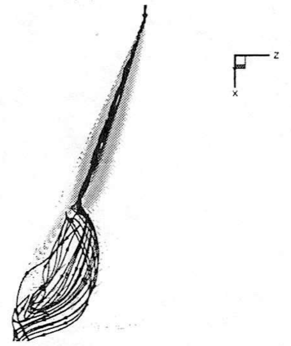

(f) $\alpha(t) = 25.1^o$

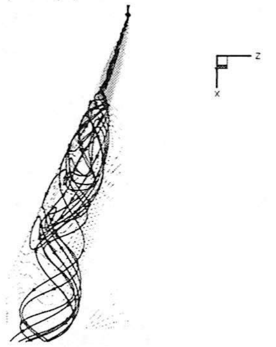

(g) $\alpha(t) = 27.0^o$

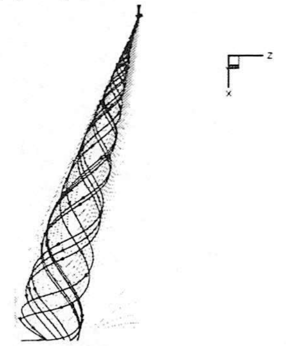

(h) $\alpha(t) = 25.1^o$

Figure 8.26: *Unsteady Breakdown Locations Within 2x3 Tunnel, k = 0.56*

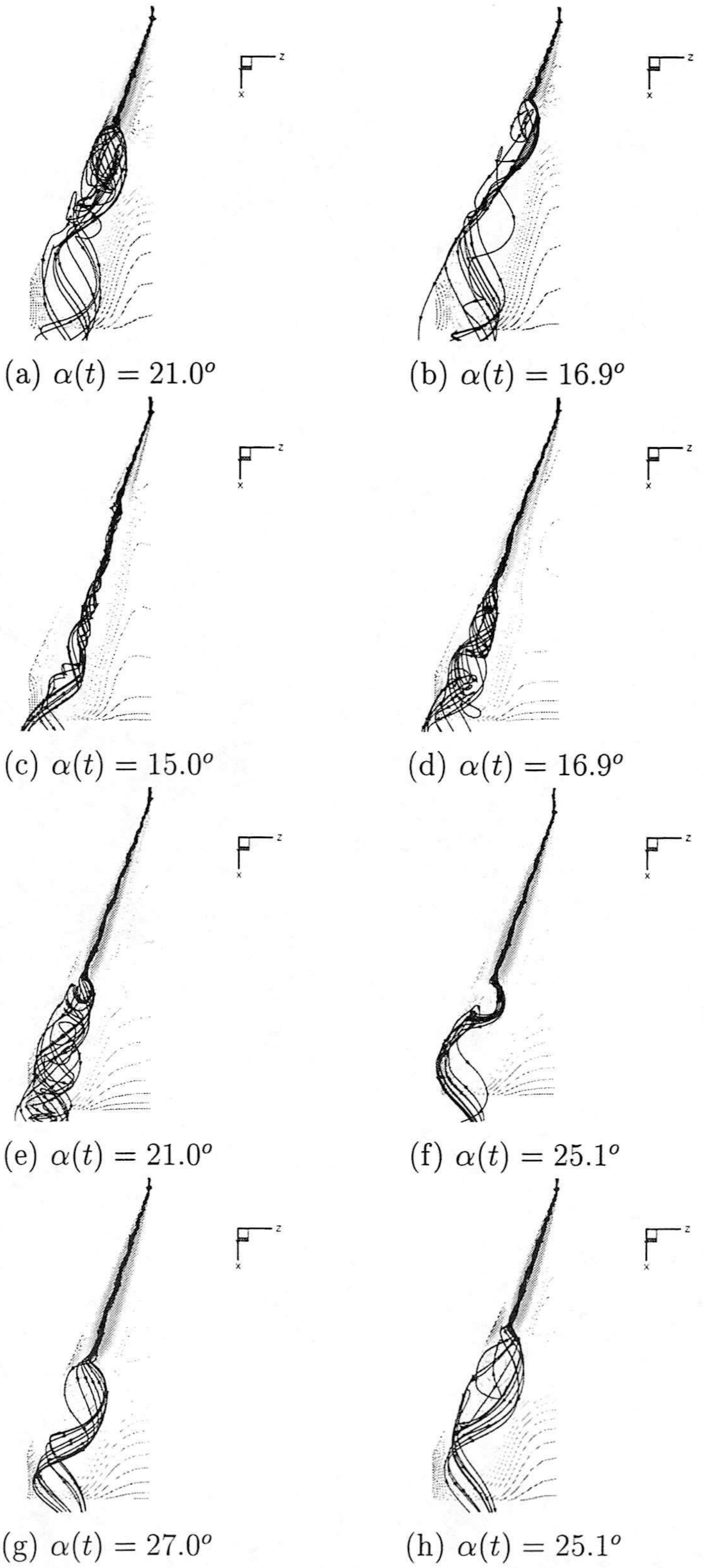

(a) $\alpha(t) = 21.0^o$

(b) $\alpha(t) = 16.9^o$

(c) $\alpha(t) = 15.0^o$

(d) $\alpha(t) = 16.9^o$

(e) $\alpha(t) = 21.0^o$

(f) $\alpha(t) = 25.1^o$

(g) $\alpha(t) = 27.0^o$

(h) $\alpha(t) = 25.1^o$

Figure 8.27: *Unsteady Breakdown Locations Within 2x3 Tunnel, k = 1.5*

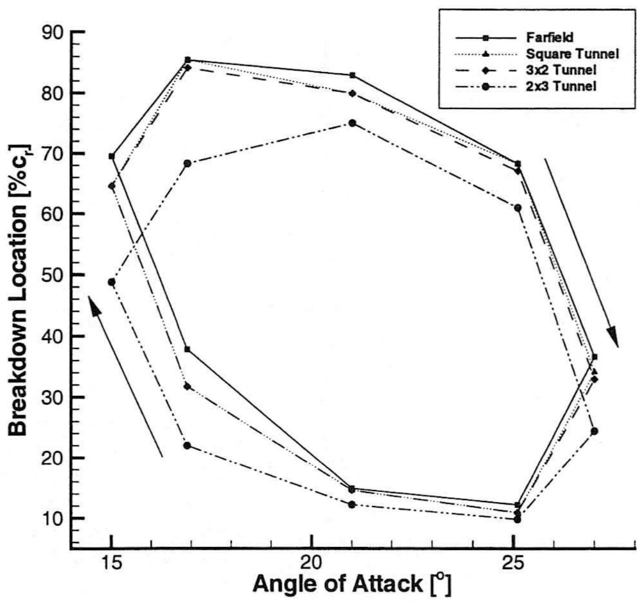

Figure 8.28: *Summary of unsteady vortex breakdown locations, k = 0.56*

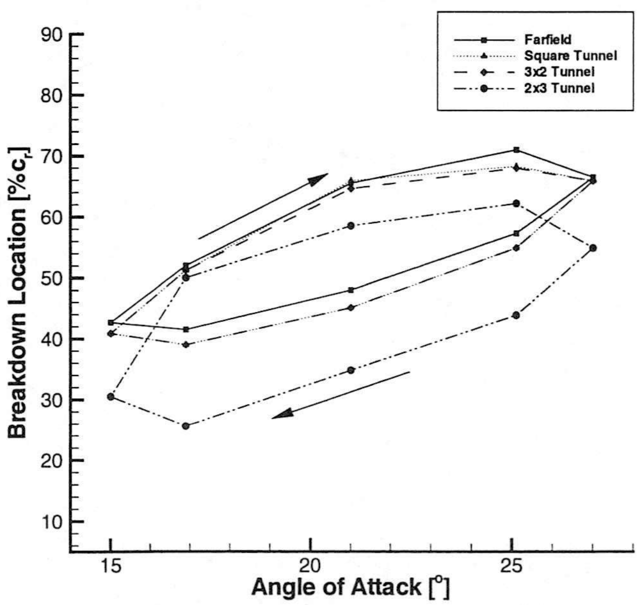

Figure 8.29: *Summary of unsteady vortex breakdown locations, k = 1.5*

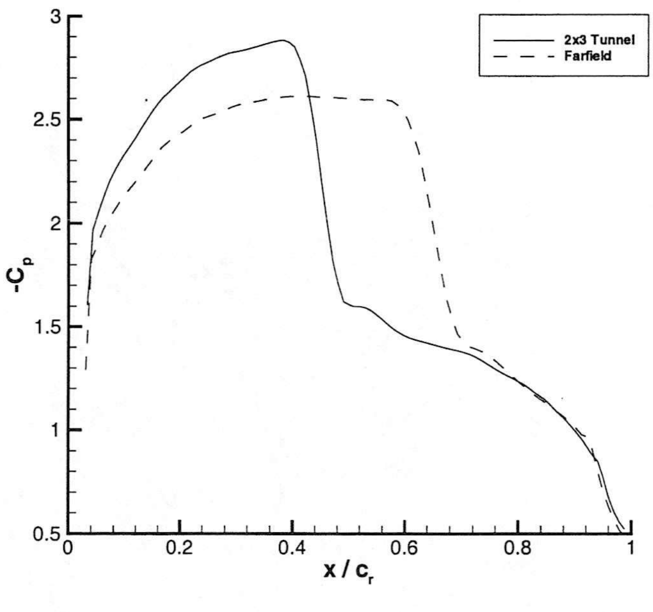

Figure 8.30: *Surface pressure distribution beneath the vortex core at 15° incidence, k = 0.56, 2x3 tunnel and farfield, Unsteady Flow*

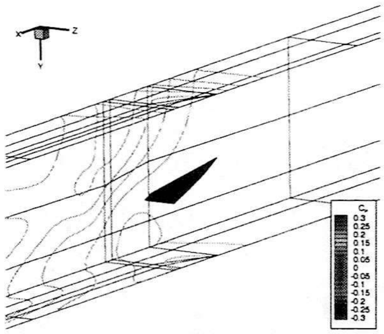

(a) $\alpha(t) = 21.0^o$

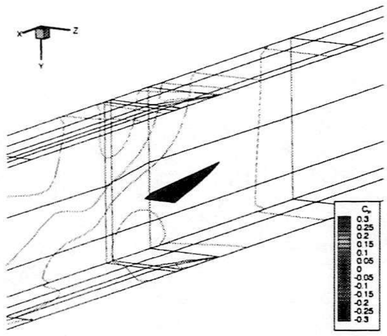

(b) $\alpha(t) = 16.9^o$

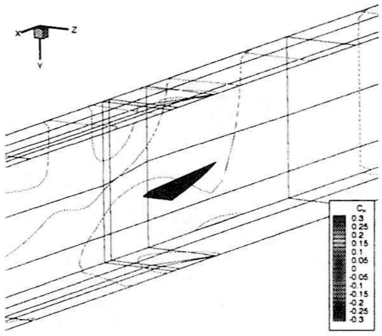

(c) $\alpha(t) = 15.0^o$

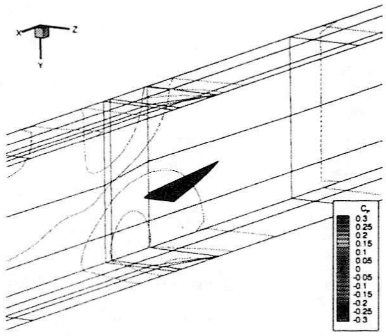

(d) $\alpha(t) = 16.9^o$

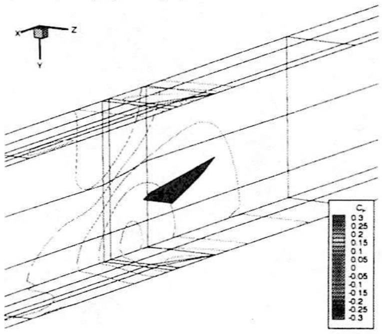

(e) $\alpha(t) = 21.0^o$

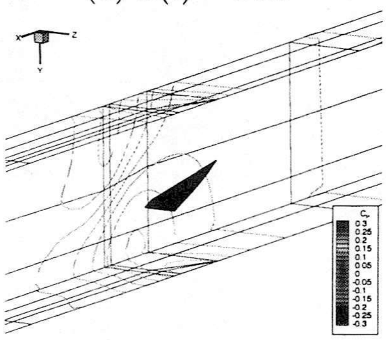

(f) $\alpha(t) = 25.1^o$

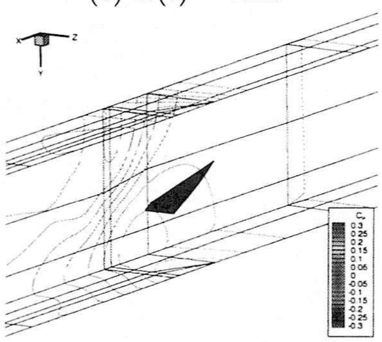

(g) $\alpha(t) = 27.0^o$

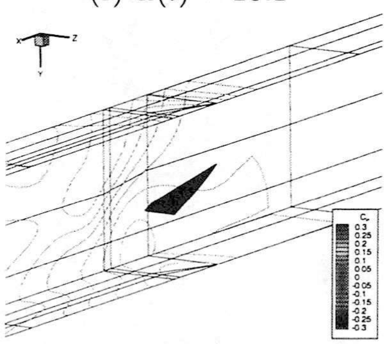

(h) $\alpha(t) = 25.1^o$

Figure 8.31: *Unsteady Wall Surface Pressures Within Square Tunnel, k = 0.56*

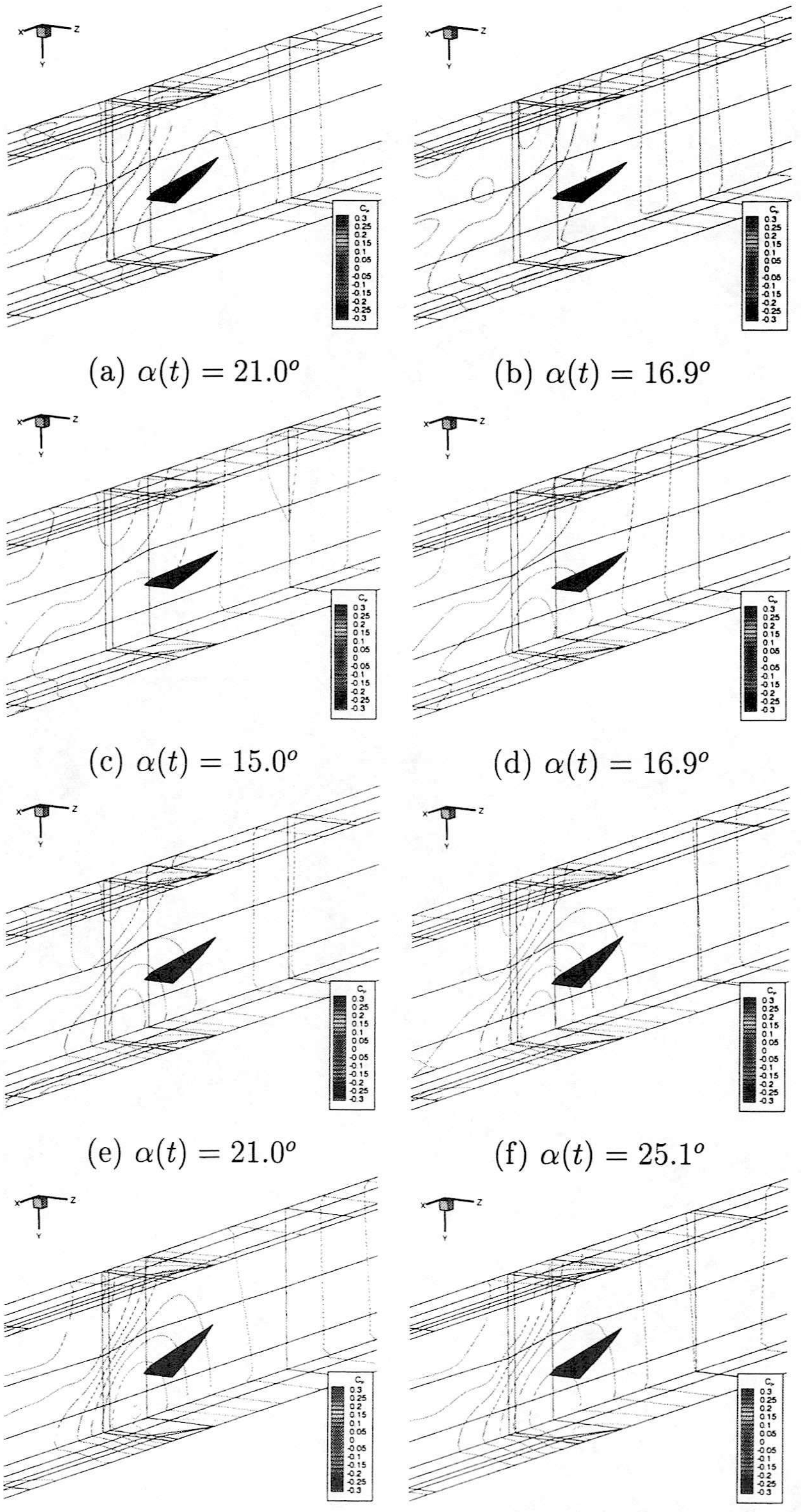

(a) $\alpha(t) = 21.0^o$

(b) $\alpha(t) = 16.9^o$

(c) $\alpha(t) = 15.0^o$

(d) $\alpha(t) = 16.9^o$

(e) $\alpha(t) = 21.0^o$

(f) $\alpha(t) = 25.1^o$

(g) $\alpha(t) = 27.0^o$

(h) $\alpha(t) = 25.1^o$

Figure 8.32: *Unsteady Wall Surface Pressures Within Square Tunnel, k = 1.5*

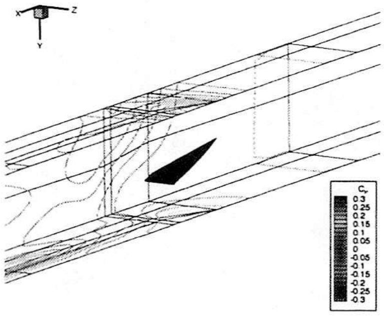

(a) $\alpha(t) = 21.0^o$

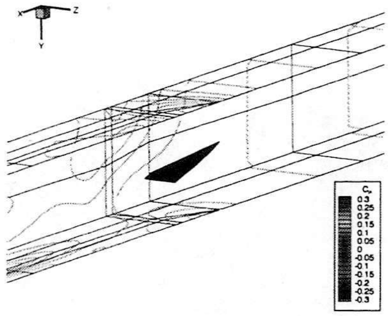

(b) $\alpha(t) = 16.9^o$

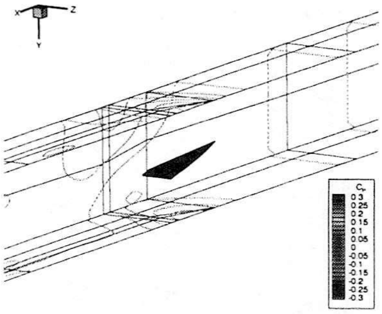

(c) $\alpha(t) = 15.0^o$

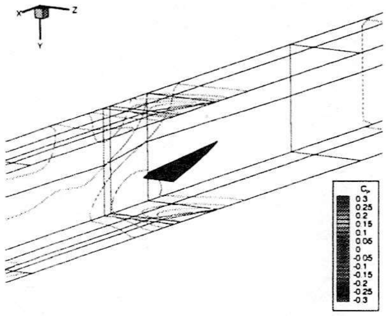

(d) $\alpha(t) = 16.9^o$

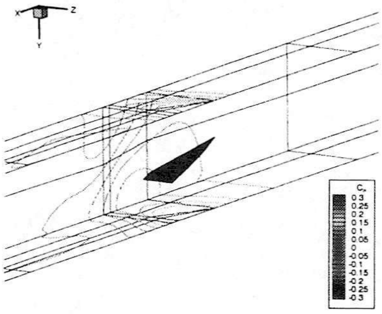

(e) $\alpha(t) = 21.0^o$

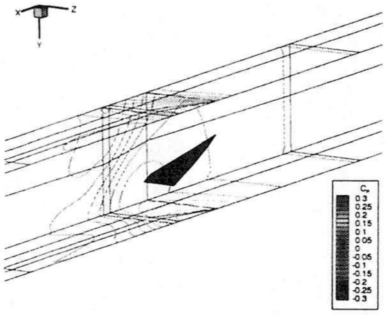

(f) $\alpha(t) = 25.1^o$

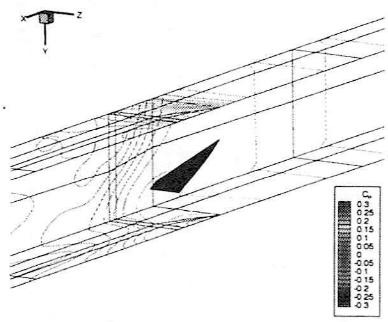

(g) $\alpha(t) = 27.0^o$

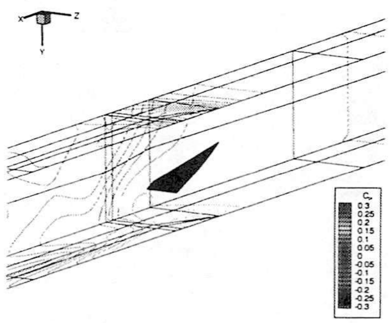

(h) $\alpha(t) = 25.1^o$

Figure 8.33: *Unsteady Wall Surface Pressures Within 3x2 Tunnel, k = 0.56*

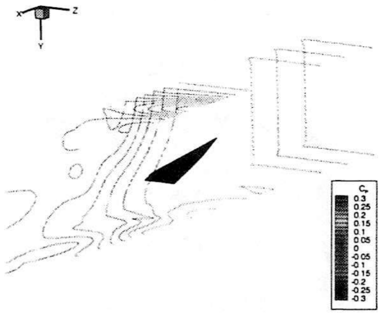

(a) $\alpha(t) = 21.0^o$

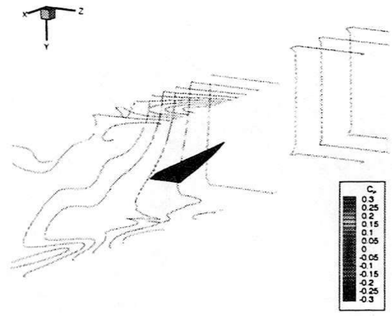

(b) $\alpha(t) = 16.9^o$

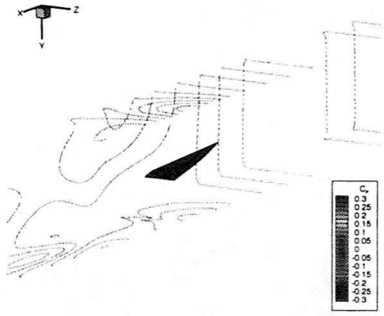

(c) $\alpha(t) = 15.0^o$

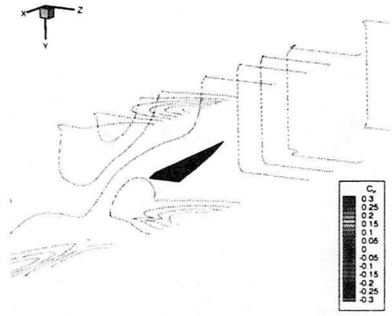

(d) $\alpha(t) = 16.9^o$

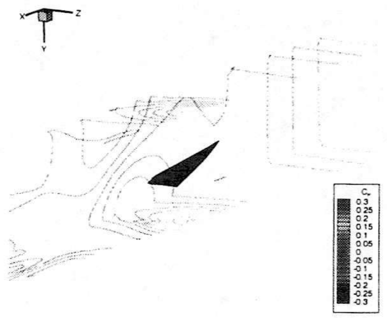

(e) $\alpha(t) = 21.0^o$

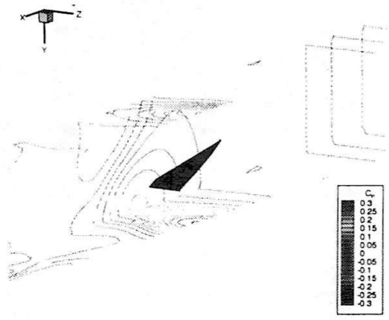

(f) $\alpha(t) = 25.1^o$

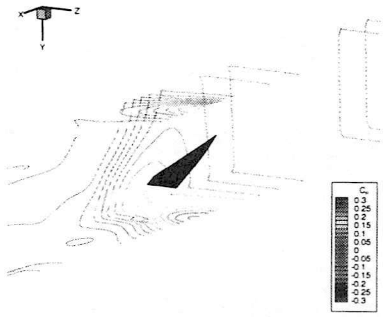

(g) $\alpha(t) = 27.0^o$

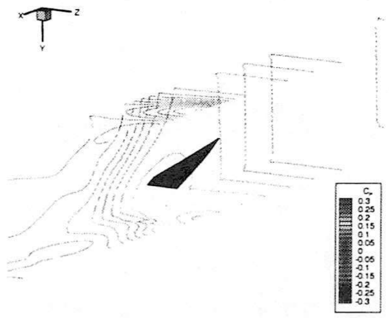

(h) $\alpha(t) = 25.1^o$

Figure 8.34: *Unsteady Wall Surface Pressures Within 3x2 Tunnel, k = 1.5*

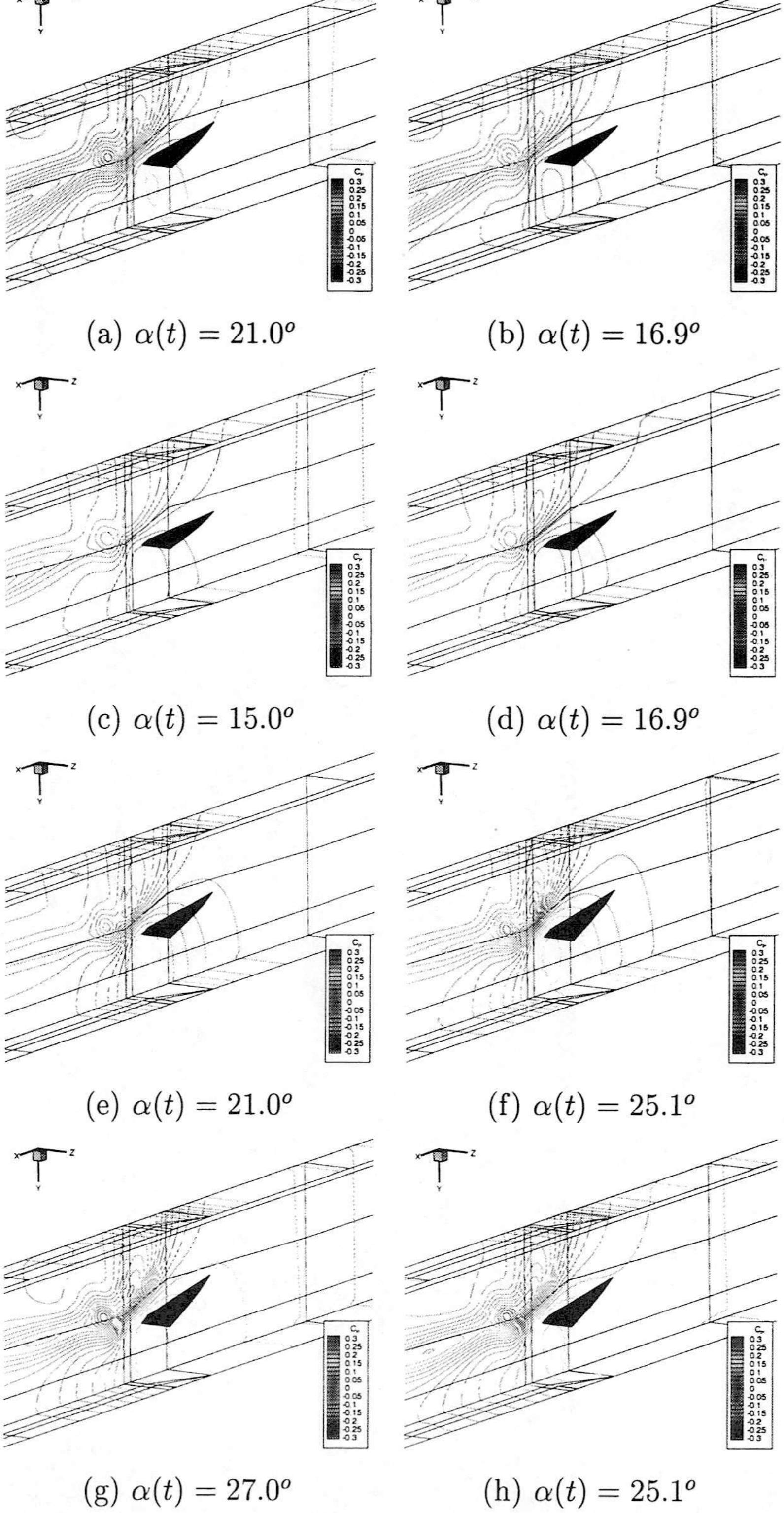

(a) $\alpha(t) = 21.0^o$ (b) $\alpha(t) = 16.9^o$

(c) $\alpha(t) = 15.0^o$ (d) $\alpha(t) = 16.9^o$

(e) $\alpha(t) = 21.0^o$ (f) $\alpha(t) = 25.1^o$

(g) $\alpha(t) = 27.0^o$ (h) $\alpha(t) = 25.1^o$

Figure 8.35: *Unsteady Wall Surface Pressures Within 2x3 Tunnel, $k = 0.56$*

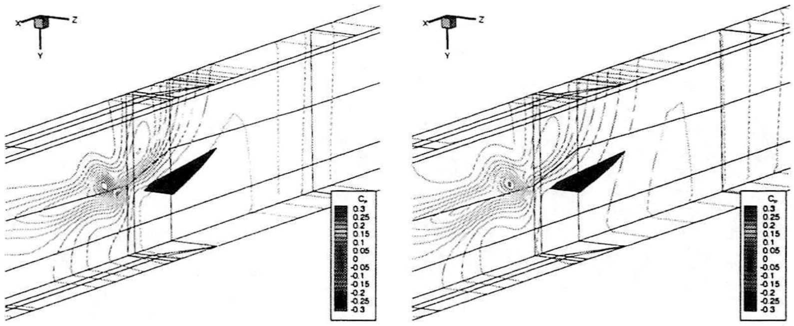

(a) $\alpha(t) = 21.0^o$ (b) $\alpha(t) = 16.9^o$

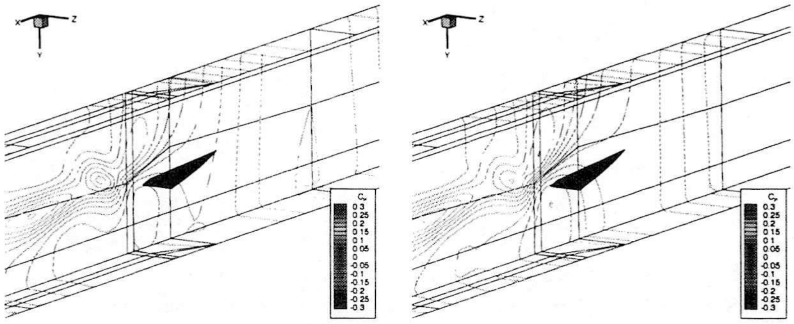

(c) $\alpha(t) = 15.0^o$ (d) $\alpha(t) = 16.9^o$

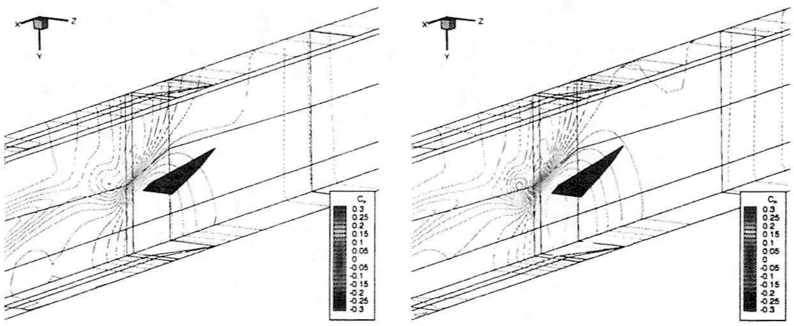

(e) $\alpha(t) = 21.0^o$ (f) $\alpha(t) = 25.1^o$

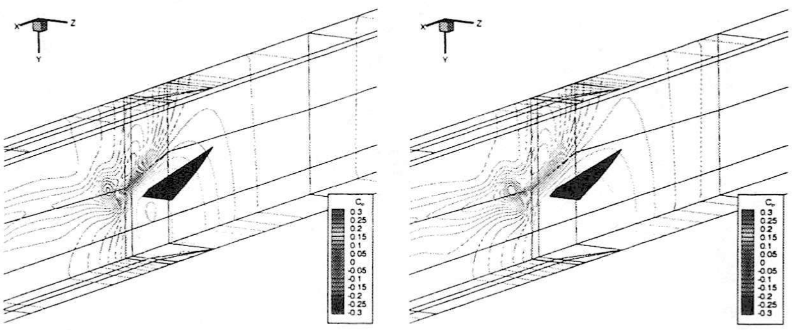

(g) $\alpha(t) = 27.0^o$ (h) $\alpha(t) = 25.1^o$

Figure 8.36: *Unsteady Wall Surface Pressures Within 2x3 Tunnel, k = 1.5*

Bibliography

[1] Garner, H. C., and Rogers, E. W. E. "Subsonic Wind Tunnel Wall Corrections". *AGARDograph 109*, 1966.

[2] Karou, A. "Separated Vortex Flow Over Slender Wings Between Side Walls - Theoretical and Experimental Investigation". *Report LR-300, Dept. of Aerospace Engineering, Delft University of Technology*, 1980.

[3] Engineering Sciences Data Unit. "Blockage Corrections for Bluff Bodies in Confined Flows". *Item 80024, London*, 1980.

[4] Frink, N. T. "Computational Study of Wind-Tunnel Wall Effects on the Flow Field Around Delta Wings". *NASA Report 87-2420*, 1987.

[5] Thomas, J. P., and Lan, C. E. "The Simulation and Correction of Wind Tunnel Wall Interference on Delta Wing Lift using Navier-Stokes and Euler Solutions". *AIAA-91-3300-CP*, 1991.

[6] Hsing, C-C. A., and Lan, C. E. "Low-Speed Wall Interference Assessment / Correction with Vortex Flow Effect". *J of Aircraft*, 34(2), March - April 1997.

[7] Weinberg, Z. "Effect of Tunnel Walls on Vortex Breakdown Location over Delta Wings". *AIAA Journal*, 30(6), June 1992.

[8] Thompson, S. A., and Nelson, R. C. "Wind Tunnel Blockage Effects on Slender Wings Undergoing Large A Amplitude Motions". *AIAA-92-3926*, July 1992.

[9] Liepmann, H. W., and Roshko, A. "Elements of Gasdynamics". *John Wiley and Sons, New York*, 1957.

[10] Arthur, M. T., Brandsma, F., Ceresola, N., and Kordulla, W. "Time accurate Euler calculations of vortical flow on a delta wing in pitching motion". *AIAA-99-3110*, 1999.

[11] Woodgate, M., Badcock, K., Richards, B. "Time accurate Euler calculations of vortical flow on a delta wing in rolling motion". *European Congress on Computational Methods in Applied Sciences and Engineering (ECCOMAS 2000)*, September 2000.

[12] Badcock, K. J., and Woodgate, M. A., Stevenson, K., Richards, B. E., Allan, M., Goura, G. S. L., and Menzies, R.,. "Aerodynamic Studies on a Beowulf Cluster". *to appear in proceedings of Parallel CFD 2001*, 2001.

[13] Loser, T. "Dynamic Force and Pressure Measurements on an Oscillating Delta Wing at Low Speeds". *Report IB 129-96/9 DLR Braunschweig*, 1997.

[14] Gortz, S., and Rizzi, A. "Computing the High-Alpha Aerodynamics of Delta Wings - Evaluation and Analysis". *AIAA-01-0115*, January 2001.

[15] Ericsson, L. E., and Beyers, M. E. "Ground Facility Interference Effects on Slender Vehicle Unsteady Aerodynamics". *J. of Aircraft*, 33(1), January-February 1996.

[16] Ericsson, L., and Beyers, M. "Aspects of Ground Facility Interference on Leading Edge Vortex Breakdown". *AIAA 2000-0978*, January 2000.

[17] Lambourne, N. C., and Bryer, D. W. "The Bursting of Leading-Edge Vortices - Some Observations and Discussion of the Phenomenon". *R&M 3282, Aeronautical Research Council, UK*, April, 1961.

[18] Gursul, I. "A Proposed Mechanism for the Time Lag of Vortex Breakdown Location in Unsteady Flows". *AIAA 2000-0787*, January 2000.